Biosensors and Bioelectronics 99 (2018) 399–415

Contents lists available at ScienceDirect

Biosensors and Bioelectronics

journal homepage: www.elsevier.com/locate/bios

Transmission surface plasmon resonance techniques and their potential biosensor applications

Chutiparn Lertvachirapaiboon[a,*], Akira Baba[a,**], Sanong Ekgasit[b], Kazunari Shinbo[a], Keizo Kato[a], Futao Kaneko[a]

[a] Graduate School of Science and Technology, Niigata University, 8050 Ikarashi 2-nocho, Nishi-ku, Niigata 950-2181, Japan
[b] Sensor Research Unit, Department of Chemistry, Faculty of Science, Chulalongkorn University, 254 Phayathai Rd. Patumwan, Bangkok 10330, Thailand

ARTICLE INFO

Keywords:
transmission surface plasmon resonance
grating-coupling surface plasmon resonance
nanohole arrays
nanoslit arrays
surface plasmon resonance image

ABSTRACT

Transmission surface plasmon resonance (TSPR) is an unusual extraordinary optical transmission that is more transparent at certain wavelengths than expected by classical theory. The three main plasmonic structures that providing this phenomenon are nanohole arrays, diffraction gratings, and nanoslit arrays. This extraordinary optical transmission phenomenon is produced as a result of surface plasmon excitations. The shifting in TSPR responses upon changing of dielectric environment at the surface of a metallic film was observed. After TSPR was discovered from metallic nanohole arrays in 1998, the number of papers about this topic rapidly increased. In the 20 years since, TSPR has been utilized to improve the detection limits, sensitivity, selectivity, and dynamic range of biosensing devices, resulting in them having greater potential for commercialization. This review gives a broad overview of the TSPR phenomenon, the development of this technique, and the typical experimental setups used to acquire TSPR signals; it also describes how they are applied in the field of research into biosensors.

1. Introduction

Surface plasmon resonance (SPR) is the strong electromagnetic oscillation of electrons that can occur at a metal/dielectric interface (Knoll, 1998; Homola et al., 1999). Because SPR is very sensitive to the refractive index of materials immediately adjacent to a thin metal film, it has been utilized in a variety of biosensor applications (Jiang et al., 2007; Sriwichai et al., 2008; Baba et al., 2010; Baba et al., 2011a, 2011b; Baba et al., 2011a, 2011b). SPR techniques have also been used to study the interactions of numerous biomolecules, including deoxyribonucleic acid, proteins, enzymes, antibodies, and antigens (Szabo et al., 1995; Kang et al., 2001; Hao et al., 2003; Su and Zhang, 2004; Soler et al., 2017). SPR can be induced using an attenuated total reflection (ATR) or diffraction grating-coupling configuration (Knoll, 1998; Homola et al., 1999). SPR-enhanced light transmission through metallic nanohole arrays was first observed in 1998 (Ebbesen et al., 1998) and was called transmission SPR (TSPR). Fig. 1 shows schematic diagrams comparing a TSPR configuration with a conventional SPR-based grating-coupling configuration. The extraordinary transmission of light through the metal-coated nanostructure results in a strong electric field (Fig. 1(A)) that is highly sensitive to the local dielectric properties of materials immediately adjacent to the metal (Baba et al., 2012; Brolo et al., 2004a, 2004b; Ebbesen et al., 1998; Lertvachirapaiboon et al., 2013; Lertvachirapaiboon et al., 2014; Thio et al., 1999; Wu et al., 2011; Yeh et al., 2010; Yeh et al., 2011; Yeh and Hillier, 2013). TSPR measurements have a lot of advantages over the conventional SPR techniques; for example, since the TSPR optical signal have no optical noise originating from reflected light, the distinctive TSPR peaks as well as dominant bright spots on a dark background indicated that enhanced transmitted light and improved signal-to-noise ratio were obtained (Singh and Hillier, 2006a, 2006b; Singh and Hillier, 2008; Yeh et al., 2011; Yeh and Hillier, 2013; Baba et al., 2012; Janmanee et al., 2012; Lertvachirapaiboon et al., 2013; Lertvachirapaiboon et al., 2014). TSPR experimental setup was a simple collinear experimental setup in which the light source, sensor chip, and detector used were aligned in a straight line without any precise angular alignment (Singh and Hillier, 2006a. 2006b; Singh and Hillier, 2008; Yeh et al., 2011; Yeh and Hillier, 2013; Baba et al., 2012; Janmanee et al., 2012; Lertvachirapaiboon et al., 2013; Lertvachirapaiboon et al., 2014). TSPR phenomenon are generally induced using metal-coated nanohole arrays and grating structures with highly uniform surfaces; the fabrication processes for TSPR

* Corresponding author.
** Co-corresponding author.
E-mail addresses: chutiparn.l@eng.niigata-u.ac.jp (C. Lertvachirapaiboon), ababa@eng.niigata-u.ac.jp (A. Baba).

http://dx.doi.org/10.1016/j.bios.2017.07.069
Received 8 April 2017; Received in revised form 9 July 2017; Accepted 28 July 2017
Available online 01 August 2017

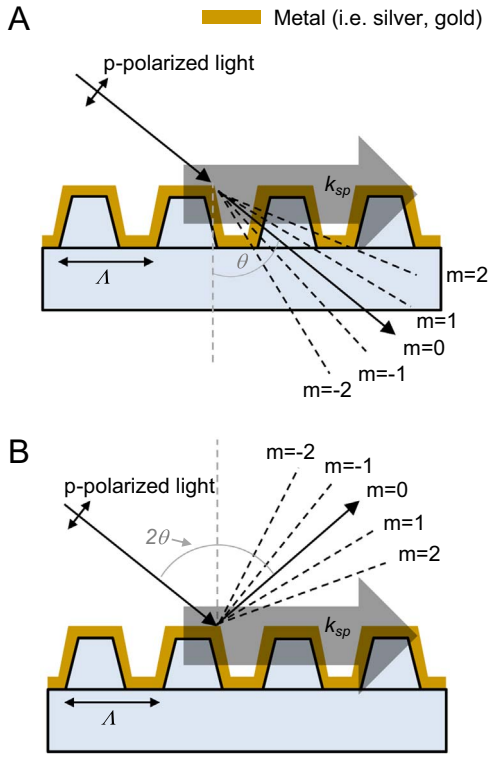

Fig. 1. (A) TSPR and (B) conventional SPR configurations. In the diagrams, Λ is the diffraction grating pitch, θ is the incident light angle, and k_{sp} is the sensitive surface plasmon wavevector.

measurements are therefore expensive. Furthermore, a spectrometer or a camera's detector is still needed for the recording of TSPR signals, as the small changes in these signals can be difficult to observe with the naked eye. Although there are some limitations to TSPR, its very high selectivity and the simple and flexible setup procedures make this technique highly useful. This ease-of-use has resulted in TSPR being used in several applications, including in biosensors; this is because these sensors can provide a simple and flexible optical configuration, provide strong spectroscopic signals, and allow for the real-time monitoring of data (Liu et al., 2004; Brolo et al., 2004a, 2004b, 2005; Leebeeck et al., 2007; Gordon et al., 2008; Sharpe et al., 2008; Escobedo et al., 2013; Wang et al., 2013; Song et al., 2015; Monteiro et al., 2016; Lee et al., 2016, Janmanee et al., 2012; Janmanee et al., 2013; Chuekachang et al., 2013a, 2013b; Chuekachang et al., 2013a, 2013b; Sriwichai et al., 2015); for example, microfluidic chip-based gold nanohole arrays have been used to monitor a biochemical affinity process involving a biotin–streptavidin system (Leebeeck et al., 2007). Furthermore, a gold nanohole array substrate was used for the multiplex detection of bacterial infections in urine (Soler et al., 2017), and a gold grating substrate was used for the immunosensing of immunoglobin G (Janmanee et al., 2012).

This review provides information regarding the development of TSPR substrates, typical experimental setups for TSPR measurements, TSPR signal enhancement done using plasmonic nanomaterials, and the various ways in which TSPR has been applied, including TSPR-enhanced fluorescent emissions for biosensor applications.

2. TSPR substrates and their development

TSPR signals have mainly been observed from the plasmonic nanostructures of (1) nanohole arrays (Ebbesen et al., 1998; Thio et al., 1999; Brolo et al., 2004a, 2004b; Wu et al., 2011), (2) diffractive nanostructures (Singh and Hillier, 2008; Yeh et al., 2011; Yeh and Hillier, 2013; Baba et al., 2012; Janmanee et al., 2012; Lertvachirapaiboon et al., 2013; Lertvachirapaiboon et al., 2014), and (3) nanoslit arrays (Chan et al., 2005; Sturman et al., 2008; Kim et al., 2009; Luo et al., 2010; Xie et al., 2010; Bian et al., 2012; Gao et al., 2014; Zhou and Guo, 2014). This section discusses the background and development of these kinds of structures. Furthermore, we also discuss non-periodic structures (Liu et al., 2004; Ren et al., 2007) that are based on TSPR phenomenon.

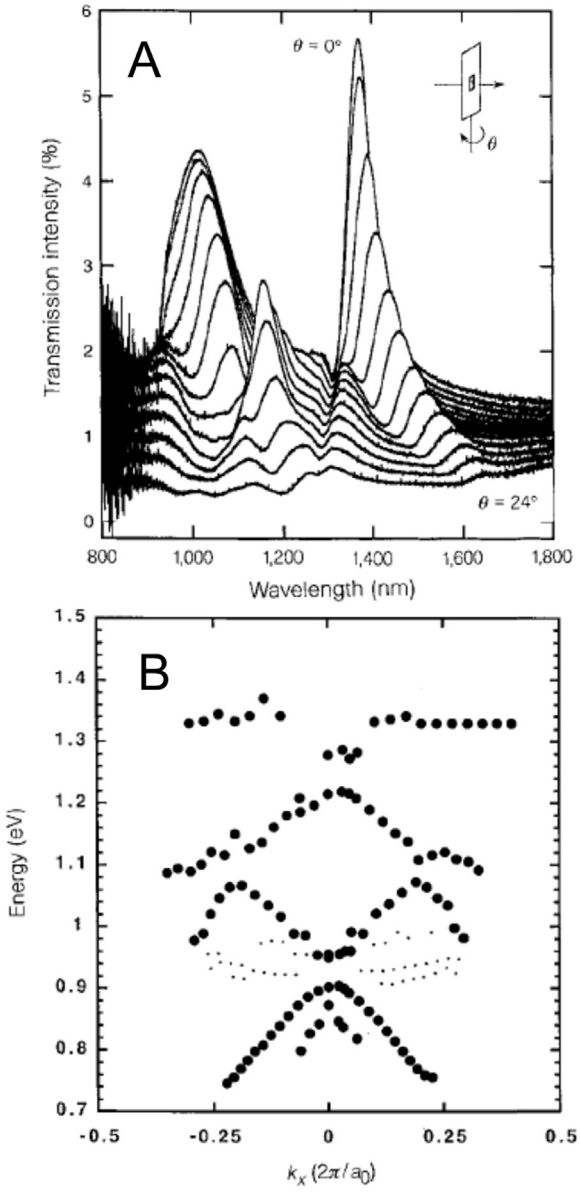

Fig. 2. (A) Transmission spectra of a square-shaped silver array (diameter = 150 nm and thickness = 200 nm) as a function of the incident angle (from 0–24°). The spectra were taken at 2° increments. (B) Dispersion curves (solid circles) along the direction of the array that were extracted from the transmission spectra shown in 2(A). The momentum k_x is in the plane of the array and is given by $k_x = (2\pi/\lambda)\sin\theta$, where θ is the incident angle of light and λ is the wavelength. The curves with small dots correspond to peaks whose amplitudes were much weaker and may not have been related to the band structure, as they do not show any significant shifts as a function of momentum (Ebbesen et al., 1998).

2.1. Nanohole arrays

Extraordinary light transmission through sub-wavelength hole arrays was first observed in 1998 (Ebbesen et al., 1998). In this first observation, sharp peaks with magnitudes ten times greater than predicted by standard aperture theory were observed in the transmitted

light. Fig. 2(A) shows the zero-order transmission spectra of a silver array (diameter = 150 nm and thickness = 200 nm) as a function of the incident angle, and Fig. 2(B) shows the dispersion curves along the direction of the array; these were extracted from the energies of the transmission peaks. These results indicated that the interaction of light with surface plasmon excitations on periodically patterned metal films results in unusual optical transmission properties. The oscillation of the surface charges on the metal surface is excited when the charges' momentum matches the momentum of the incident photon and grating; this can be seen in the following equation:

$$k_{sp} = k_x \pm nG_x \pm mG_y$$

where k_{sp} is the surface plasmon wavevector, $k_x = (2\pi/\lambda)\sin\theta$ is the component of the wavevector of an incident photon in a grating plane, and $G_x = G_y = 2\pi/a_o$ are grating momentum wavevectors for a two-dimensional array structure. Significant shifts in the transmission peaks as a function of momentum, k_x, can be seen in Fig. 2(B) (indicated by the solid circles); however, some of the transmission bands showed negligible change as a function of momentum (indicated by the small dots in Fig. 2(B)) (Ebbesen et al., 1998).

In order to gain further insight into the extraordinary optical transmission that occurs in metallic nanohole arrays, several other parameters were studied; these parameters included the refractive index (Krishnan et al., 2001; Barnes et al., 2004), the polarization of incident light (Barnes et al., 2004), and the role of the cylindrical structure (Haftel, 2006). In 2001, Ebbesen *et al.* reported that TSPR provided a very strong signal when surface plasmon modes on either side of a metallic film were matched (Krishnan et al., 2001). Fig. 3 shows the experimental transmission spectra of a gold film on a quartz substrate ($\varepsilon_S = 2.31$) as a function of the refractive index of a dielectric layer (ε_L) on the gold film (Krishnan et al., 2001). In this experiment, the thickness of the gold film was 250 nm, the hole diameter was 200 nm, and the lattice constant was 600 nm. A numerical simulation corroborated the experimental results as the strongest transmission intensity was observed when the refractive indices of both sides of the film were similar (*i.e.*, $\varepsilon_L \sim \varepsilon_S$).

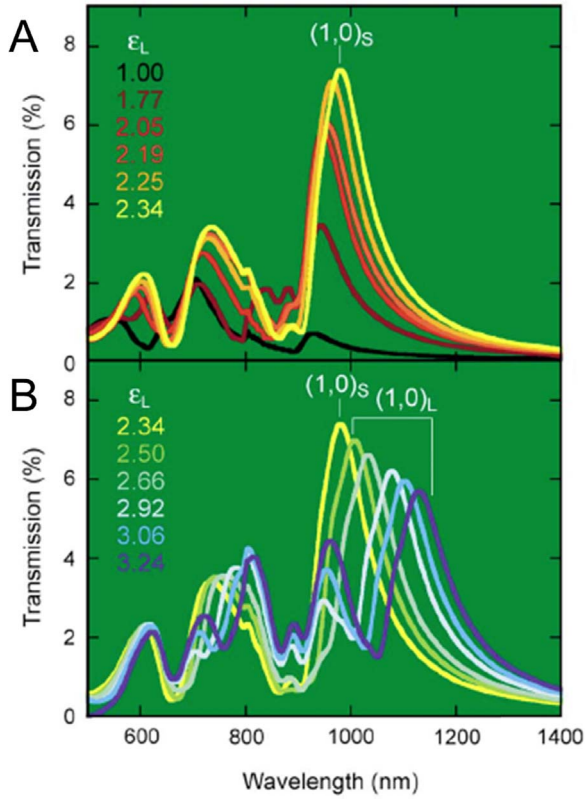

Fig. 3. Experimental zero-order transmission spectra of a gold film on a quartz substrate ($\varepsilon_S = 2.31$) as a function of the refractive index of a dielectric layer (ε_L) on the gold film. The thickness of the gold film was 250 nm, the hole diameter was 200 nm, and the lattice constant (a_0) was 600 nm: (A) $\varepsilon_L \leq \varepsilon_S$ and (B) $\varepsilon_L \geq \varepsilon_L$. ε_S is the dielectric constant of the quartz substrate, while ε_L is the dielectric constant of the gold film (Krishnan et al., 2001).

After the extraordinary optical transmission phenomenon was observed in metallic nanohole arrays, studies were carried out on a variety of different structures that were felt to be potential candidates for this phenomenon. One study compared TSPR signals from circular (cylindrical) and rectangular nanohole arrays (Koerkamp et al., 2004); it was found that the TSPR intensity was stronger when the rectangular array was used, and that this array resulted in an order of magnitude increase in sensitivity with respect to shifts of the TSPR peak. Another study looked at what effect the number of holes and the arrangement of the holes had in terms of inducing extraordinary optical transmission (Degiron et al., 2004). In this study, a silver film with a shallow cylindrical hole showed an unexpected result; namely, an observable surface plasmon mode from a single sub-wavelength ($\lambda > 2d$) cylindrical hole. This surface plasmon mode was a localized electric field oscillating perpendicular to the incident electric field. A one-dimensional structure composed of nanoholes that formed a linear chain of sub-wavelength holes was also investigated (Bravo-Abad et al., 2004). The results from this study indicated that when the number of linear chains is increased, the transmission peak is shifted toward longer wavelengths; they found that this was due to a reduction in the lateral confinement. They also found that the amplitude increased when the number of linear chains was increased. A two-dimensional structure of nanohole arrays ($N \times N$) was also studied (Lezec and Thio, 2004). In this study, scanning electron microscopy (SEM) micrographs of nanohole arrays with N = 1, 4, and 9 consisting of cylindrical holes (diameter = 150 nm) in a silver film (thickness = 175 nm) layered on glass coated with index-matching fluid are shown in Fig. 4(A)–(C), respectively. The transmission intensities and their corresponding transmission coefficients per hole are shown in Fig. 4(D) and (E), respectively. A slight blue shift can be observed in these figures, and an increase in the per-hole transmission coefficient can be seen when N is increased. These results indicate that there is a propagating electric field on the glass substrates coated with the index-matching fluid.

Recently, complex hole structures have become a topic of interest (Haftel, 2006; Li et al., 2016; Clark and Cooper, 2012), and a cylindrical ring structure has been found to exhibit extraordinary optical transmission (Haftel, 2006). The study that found this noted that when the ring structure became narrower, the TSPR intensity increased, and the TSPR peak shifted to longer wavelengths. These results indicated that the cylindrical insulator–metal interface of the ring also showed the propagating surface plasmon. More recently, asymmetric cross-shaped nanoapertures in an aluminum thin film were found to exhibit very strong tunable optical transmission properties (Li et al., 2016). The plasmonic cavity exhibited a dual-color characteristic, which was controlled by the polarization of white light and could be tuned by varying the critical dimensions of the cavity's geometry and the array's periodicity. This finding is expected to impact future display, printing, high-density optical data storage, and imaging and filtering technologies (Clark and Cooper, 2012; Li et al., 2016).

2.2. Grating structures

In 2008, Singh and Hillier observed the TSPR phenomenon occurring due to a gold-coated, transparent diffraction grating (Singh and Hillier, 2008). With this plasmonic structure, they were able to observe narrow peaks and tune them over a wide wavelength range (visible–near-infrared (NIR) region) by rotating the plasmonic structure. The observed TSPR peaks corresponded with the surface plasmon conditions at the metal/air interface. The extraordinary optical transmission phenomenon observed in this study was also governed by the

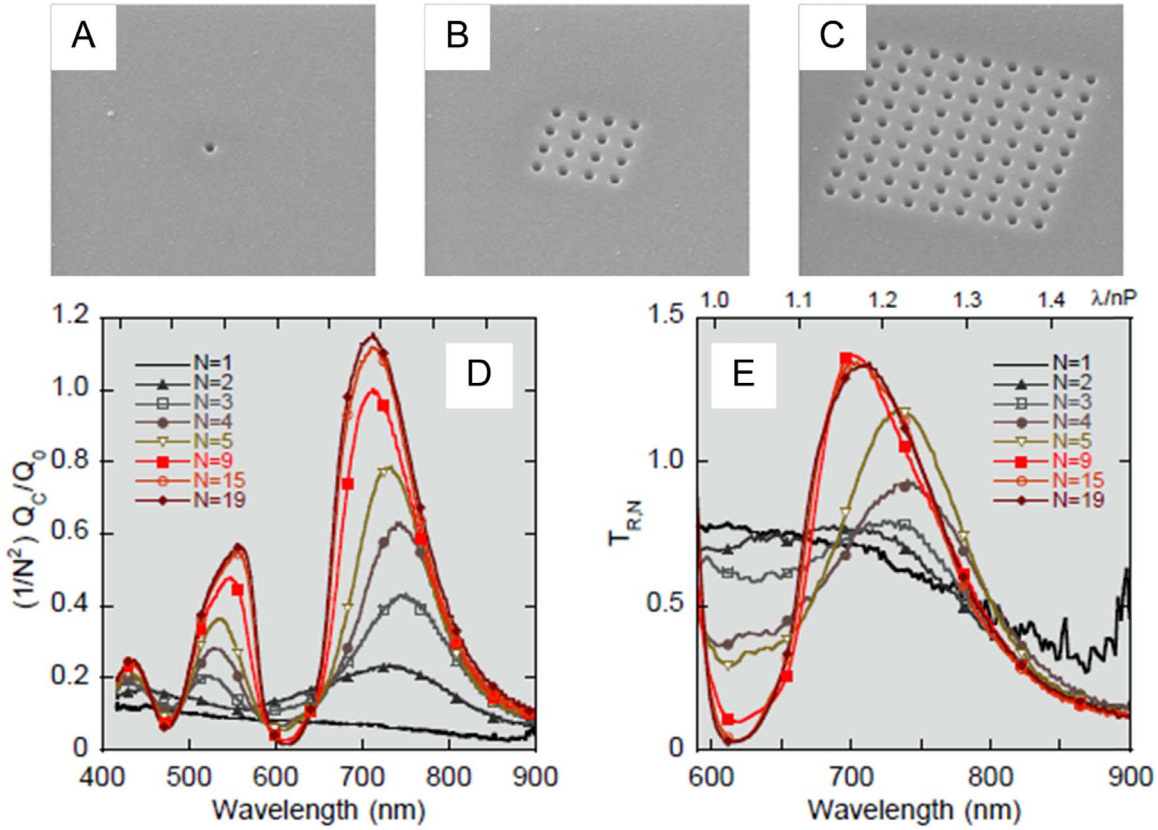

Fig. 4. (A)–(C) SEM images of $N \times N$ square array structures for N = 1, 4, and 9. (D) Transmission spectra of silver films containing cylindrical nanoholes as a function of N, and (E) the corresponding transmission coefficient per hole (Lezec and Thio, 2004).

momentum matching condition between the surface plasmons in the grating plane and the grating momentum wavevector. The experimental setup used in this study to acquire the TSPR spectrum required transmission alignment; in brief, a light source was passed through a collimating lens, linear polarizer, and pinhole before the TSPR spectrum was recorded by both a fiber optic spectrometer and a camera's detector (more information about this experimental setup will be provided in an experimental section). A typical transmission spectrum for a gold-coated grating substrate as a function of the angle of incidence of the excitation light is shown in Fig. 5 (Singh and Hillier, 2008). The changes in the TSPR signal were confirmed to be sensitive to the dielectric function *via* the deposition of different self-assembled monolayers of hexanethiol (n = 6, thickness = 0.60 nm), decanethiol (n = 10, thickness = 1.04 nm), and octadecanethiol (n = 18, thickness = 2.14 nm) on the gold grating substrates. The TSPR peak was found to shift linearly toward longer wavelengths when the chain length of the hydrocarbons was increased. Singh and Hillier also used a gold-coated grating substrate for the immunosensing of bovine serum albumin (BSA) and anti-BSA system. Their work was the first to systematically explain how the TSPR phenomenon occurs on conventional grating structures, and it was also the first to use a TSPR substrate for a biosensor application.

In 2010, the effect of the pitch of a grating was investigated (Yeh et al., 2010). In this study, photographic images and their corresponding optical transmission spectra at 630 nm at various x-positions along the center of a gold-coated grating substrate were recorded (both the pitch and the amplitude of the gold-coated grating structure were gradually increased); their results can be seen in Fig. 6(A) and (B). A compilation image of TSPR spectra as a function of the x-position of this substrate is shown in Fig. 6(C), with the series of peaks corresponding to diffraction modes.

The TSPR images obtained from a gold-coated grating substrate at a normal angle were recorded, while the dielectric properties on the gold grating's surface were changed by changing the thickness of a SiO film. The feature of the TSPR image for the diffraction mode m = +1 using p-polarized light changed significantly, while the transmission signal obtained using s-polarized light was barely observable and did not change significantly (Yeh et al., 2011). This work presented a simple method for tracking adsorption, thin-film formation, and changes in the dielectric properties on the gold surface, and it also provided a novel detection method for recording TSPR images, as it was now possible to detect them using a camera. In 2013, Yeh and Hillier presented a TSPR dispersion image of diffraction-based tracing through a gold-coated grating structure. This image represented a dense compilation of measurement TSPR spectra as functions of both wavelength and the angle of incidence; it was found that this could be used to specify plasmon modes including their associated diffraction order at the coupling and decoupling interfaces of the front and back sides of the substrate, respectively (Yeh and Hillier, 2013). TSPR excitation could be fine-tuned by the electrochromism of conducting polymer thin films (Baba et al., 2012). Conducting polymers of polyaniline (PANI) and poly(3,4-ethylenedioxythiphene) (PEDOT) were deposited on the surface of a thin, gold grating, and an electrochemical-transmission surface plasmon resonance (EC-TSPR) measurement was carried out by irradiating white light on the conducting polymer thin-film gold grating surface and detecting the light transmitted from the back side; while this was done, the morphology and the doping state of the conducting polymer were electrochemically controlled. It can be seen in Fig. 7(A) and (B) that there were significant changes in the TSPR spectrum for both PANI and PEDOT; these changes were found at incident angles of 35° and 25°, respectively, when an electrochemical potential was applied. The PANI thin film showed an on/off switching behavior for the TSPR spectra, while the PEDOT thin film exhibited wavelength tuning (Baba et al., 2012). It was therefore shown that the TSPR spectrum obtained using EC-TSPR exhibited different excitation wavelengths for different grat-

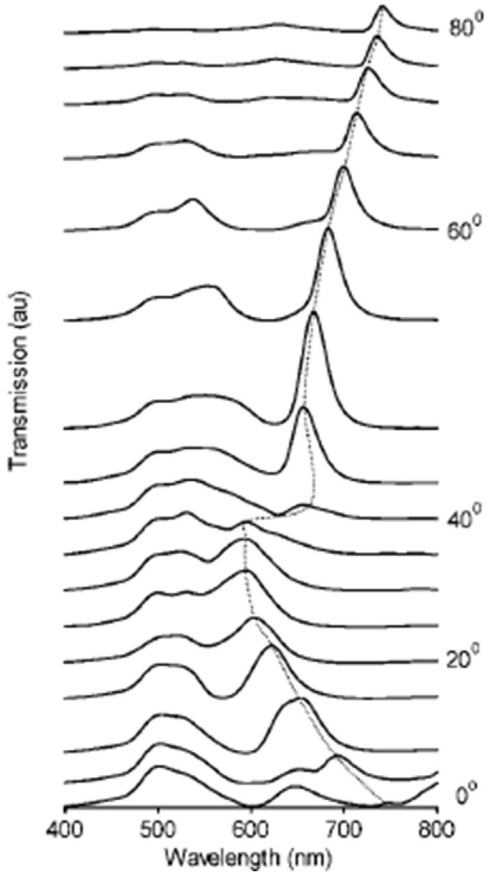

Fig. 5. Transmission of p-polarized light through a 45-nm-thick gold film on a grating for incident angles of 0–80°. The dotted line shows the maxima in the enhanced transmission peaks (Singh and Hillier, 2008).

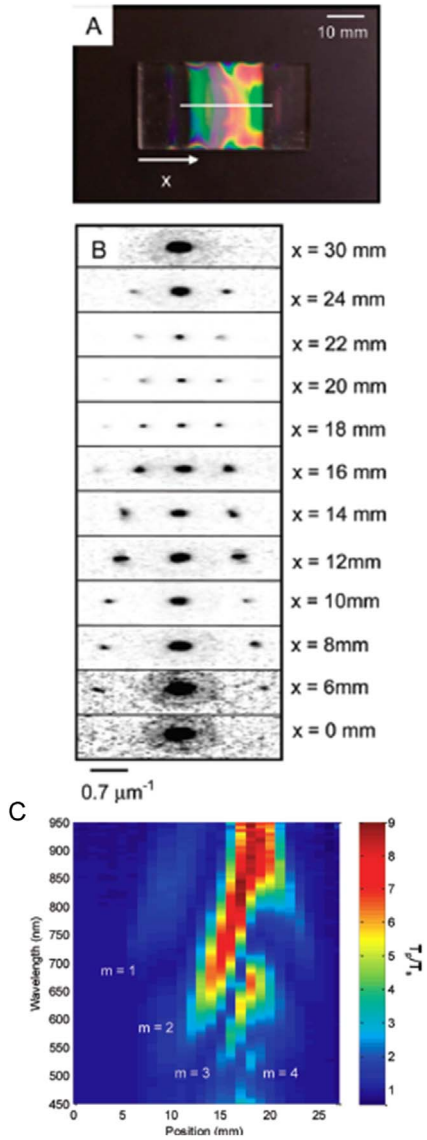

Fig. 6. (A) Optical image showing the reflection from a chirped diffraction grating. The *x*-position indicates the bend axis. (B) Optical diffraction images (inverted contrast) acquired from the transmission of 630 nm of light for various degrees of bending of the *x*-position along the center of the diffraction grating. (C) An image of the transmission spectra (T_p/T_s) as a function of the bending of the *x*-position between $x = 0$ and $x = 19$ mm along the center of a gold-coated diffraction grating (the transmission spectrum was recorded at 1-mm intervals along the *x*-axis). *m* represents the diffraction order of each transmission peak in the figure (Yeh et al., 2010).

ing structures that were under the same electrochemical condition. In a different study, a poly(3-aminobenzoic acid) (PABA) thin film was electropolymerized on a gold-coated grating substrate, and an *in situ* study of the TSPR phenomenon was carried out under different doping states (Sriwichai et al., 2015). The TSPR peak position of the PABA thin film on the gold-coated grating structure obtained from a BD-R disc during an applied potential between 0.15 and 0.5 V was located between 660 and 680 nm, while that of the PABA thin film on the gold-coated grating structure obtained from a DVD-R disc was located between 745 and 760 nm.

Nanoslit array structures have been important in the development of TSPR substrates (Chan et al., 2005; Sturman et al., 2008; Kim et al., 2009; Luo et al., 2010; Xie et al., 2010; Bian et al., 2012; Gao et al., 2014; Zhou and Guo, 2014). In 2005, a strong TSPR phenomenon was observed for an aluminum nanoslit array structure (Chan et al., 2005). In that study, the optical transmission through a nanoslit array structure was found to be as high as 80% at the plasmon resonance wavelength. Theoretical calculations made by the study corroborated the results, and they suggested that the strong electric field originated from an enhanced electric field on the metal surface; this enhanced electric field was caused by the propagation of surface plasmons. Another structure of interest was found to be a double-layer gold slit array structure (Xie et al., 2010). The optical transmission properties of this structure were found to have been caused by SPR and localized waveguide resonance. The extraordinary transmission signal obtained from this material was dependent on the separation between the structure's layers as well as on the lateral displacement between the two metallic nanoslit layers. Furthermore, it was also shown that the extraordinary optical transmission properties under transverse-electric polarization were due to Fabry–Perot cavity resonances; a dielectric waveguide mode was also observed (Crouse and Keshavareddy, 2007; Lu et al., 2008; Bian et al., 2012; Gao et al., 2014).

Recently, the periodic structures providing TSPR phenomenon have increased in complexity (Petefish and Hillier, 2015; Zhang et al., 2015; Lee et al., 2015c). A multi-pitched diffraction grating was developed using laser interference lithography (Petefish and Hillier, 2015). After the silver was coated, this substrate provided multiple simultaneous plasmon peaks directly associated with its own structure and was exploited for surface-enhanced infrared absorption. TSPR has also been observed from tapered multilayer slit structure (Zhang et al., 2015). Simulation results for this structure indicated that the thin dielectric layers sandwiched between the two silver layers (Fig. 8(A-1)) provided a significant improvement in the transmission efficiency in the infrared region that depended upon the thickness of the spacer

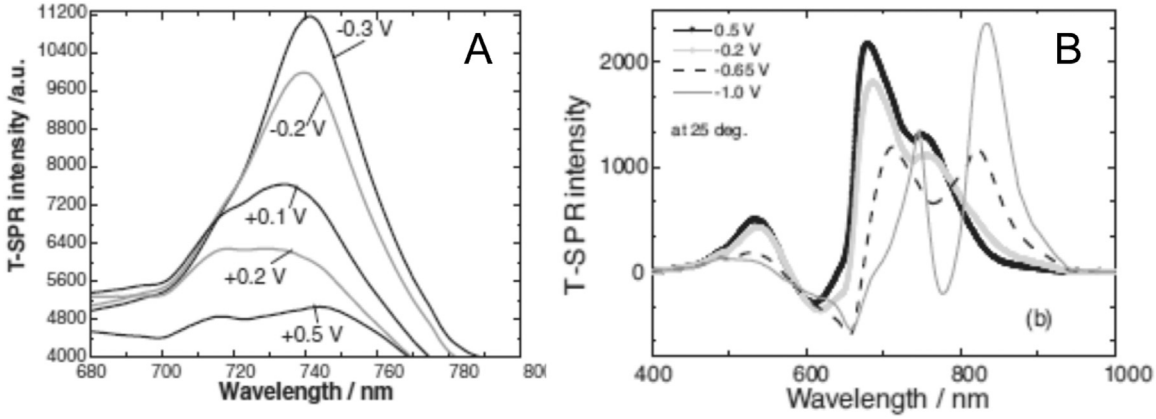

Fig. 7. (A) TSPR spectra of a PANI thin film on a gold-coated grating substrate in an aqueous H_2SO_4 solution for various constant potentials (−0.3, −0.2, +0.1, +0.2, and +0.5 V) at an incident angle of 35°. (B) TSPR spectra of a PEDOT thin film on a gold-coated grating substrate in an aqueous tetrabutylammonium hexafluorophosphate solution for various constant potentials (−1.0, −0.65, −0.2, and +0.5 V) at an incident angle of 25°. The PANI thin film exhibits on/off switching for the TSPR spectra, while the PEDOT thin film shows wavelength tuning (Baba et al., 2012).

layer, as shown in Fig. 8(A-2). Another example of complex structure providing extraordinary optical transmission properties was a capped gold nanoslit array structure made from a thermally embossed, nanoimprinted polymer film; a schematic diagram of this structure is shown in Fig. 8(B-1) (Lee et al., 2015c). This substrate was found to produce a very sharp asymmetric resonance under excitation with p-polarized light. Typical measured (Fig. 8(B-2)) and calculated (Fig. 8(B-3)) transmission spectra of a 500-nm-period gold nanostructure with different structural parameters in water at normal incident angles are shown in Fig. 8(B).

2.3. Non-periodic structures

Non-periodic structures based on nanohole structures have also been observed to exhibit TSPR phenomenon (Liu et al., 2004; Ren et al., 2007). The earliest example of this kind of structure was found using randomly placed nanocavities. The nanocavities with diameters of 200 nm were randomly located in a 70-nm-thick gold film that was fabricated using electron beam lithography; the structure was developed so as to enhance fluorescence emissions in biosensor applications (Liu et al., 2004). The enhanced fluorescent signal of this substrate was

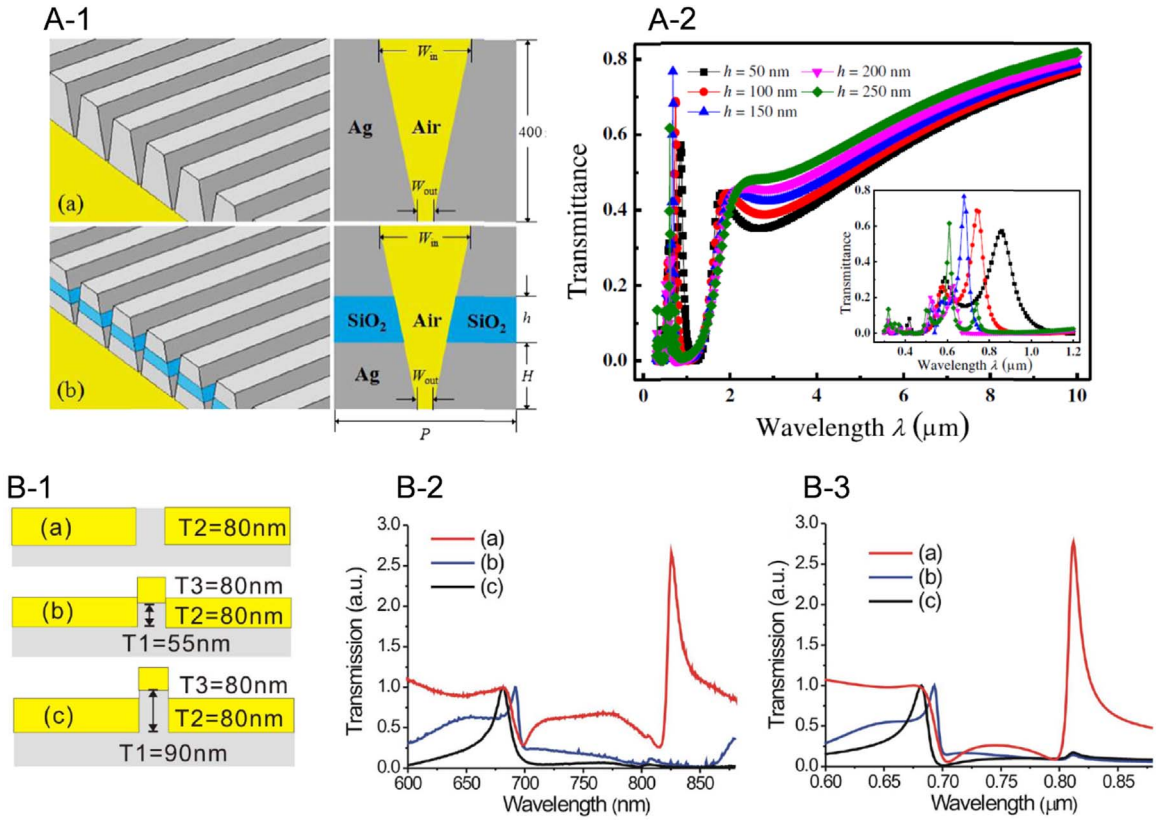

Fig. 8. (A-1) Schematic diagrams of (a) a tapered monolayer slit structure and (b) a tapered multilayer slit structure separated by a SiO_2 layer. (A-2) Simulated transmission spectra of the tapered multilayer slit structure as a function of the SiO_2 layer thickness (Zhang et al., 2015). (B-1) Schematic diagram depicting the geometrical parameters of (a) a nanoslit structure, (b) a long-cavity capped nanoslit structure, and (c) a short-cavity capped nanoslit structure. (B-2) Measured transmission spectra of 500-nm-period gold nanostructures with different structural parameters in water at normal incident angles and their corresponding calculated transmission spectra (Lee et al., 2015c).

originated from the excitation of surface plasmons at the gold/air interface caused by the incident light that was evanescently coupled through the nanocavities. This substrate was exploited for the real-time monitoring of 20-base pair-long oligonucleotides in solution. Another example of a TSPR substrate with a non-periodic structure is a quadrate hole array substrate (Ren et al., 2007); although this kind of structure is technically uniform, this study investigated the TSPR phenomenon while rotating the substrate. The extraordinary transmission signal obtained as a result of this unsymmetrical periodicity demonstrated the influence of propagating surface plasmon polaritons, as the transmission signals of this substrate were tuned based on changes to the incident light. The transmission intensity and the ratio between the transmission efficiencies of the horizontal and vertical polarized light could be continuously tuned by rotating the quadrate hole array.

3. Experimental setups for TSPR measurements

3.1. Spectroscopic measurements

TSPR spectra were obtained using a TSPR system equipped with a fiber optic spectrometer (HR 4000, Ocean Optics) and a white light source (LS-1 tungsten halogen, Ocean Optics). The substrates were mounted on a rotation stage. White light was then passed through a linear polarizer, and the TSPR signals were detected by the fiber optic spectrometer (Lertvachirapaiboon et al., 2013, 2014). Surface plasmons were excited at the metal grating–dielectric interface *via* irradiation of white light at fixed angles of incidence. Fig. 9(A) shows a schematic diagram of the sample structure. In order to obtain normalized spectra, the TSPR signal was obtained by subtracting the p-polarized light intensity from the s-polarized light intensity. Fig. 9(B) shows the TSPR spectra for a gold-coated grating substrate measured at incident angles of 25–40° in water. The TSPR peaks were observed between 700–800 nm. The sensitivity of the TSPR peak shift depended on the incident angle, which is indicative of propagating surface plasmons on the gold grating's surface. Several experimental setups similar to the one described in this paper also showed strong TSPR signals in the visible–NIR region (Singh and Hillier, 2008; Janmanee et al., 2012; Baba et al., 2012; Sriwichai et al., 2015).

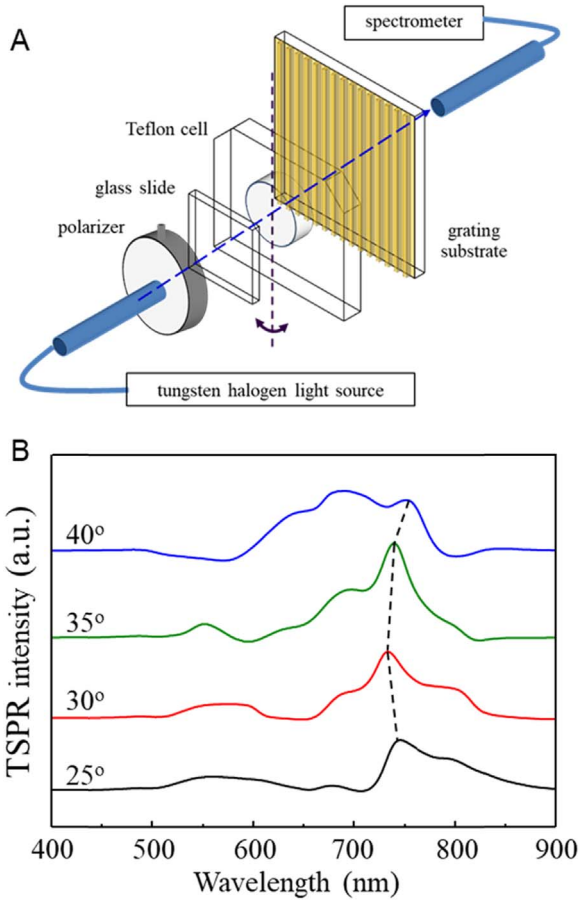

Fig. 9. (A) Schematic diagram of the experimental setup used for recording a TSPR spectrum. (B) Typical TSPR spectra at the incident angles of 25–40° for a gold-coated grating. The TSPR signal was obtained by subtracting the p-polarized light intensity from the s-polarized light intensity.

3.2. TSPR image acquisition

3.2.1. TSPR image-based diffraction image (large area, long working distance)

TSPR images have been obtained using a camera's detector. In 2010, the first TSPR image-based diffraction of a gold-coated grating structure was reported upon (Yeh et al., 2010). In 2011, TSPR signals from imaging and spectroscopic techniques that were comparable were further studied by the same group (Yeh et al., 2011). Their results showed very strong transmission signals and supported the SPR phenomenon that are expressed along the direction of the grating plane and the grating momentum wavevectors (Yeh et al., 2010; Yeh et al., 2011). Fig. 10(A) shows a typical TSPR imaging experimental setup for the study of TSPR phenomenon based on a diffraction grating system. Fig. 10(B-3), meanwhile, shows a strong and sharp optical transmission signal from the gold-coated grating substrate (denoted by the asterisk) under p-polarized light (Yeh et al., 2011).

3.2.2. TSPR image-based near-field effect (small area, short working distance)

The transmission phenomenon described in this sub-section originated from plasmonic resonances. A strong extraordinary optical transmission was obtained from a metal nanostructure substrate using a unique optical setup (Lee et al., 2007, 2015a, 2015b, 2017). The investigation of single particles *via* total internal reflection scattering (SD-TIRS) dual modes coupled with a transmission grating (TG) imaging system was demonstrated (Lee et al., 2015a, 2015b, 2017). A 671-nm solid-state continuous wave laser and a 405-nm laser were used as excitation sources. An electron-multiplying cooled charge-coupled device camera (512 × 512 pixel imaging array, QuantEM 512SC, Tucson) was used to record the images. The exposure time used was 50 ms. A TG beam splitter with 70 grooves/mm (Edmund Optics Inc.) was mounted in front of the camera so as to disperse the scattering caused by the plasmonic nanoparticles (i.e., AgNPs, AuNPs, and gold nanopads). A photographic image and a schematic of the experimental setup are shown in Fig. 11. 100-nm-diameter gold nanopads were used in this experiment; they are a substrate typically used to provide extraordinary optical transmission images. Difference interference contrast (DIC) and SEM images of the gold nanopads are shown in Fig. 11(C). This system was utilized for the quantitative screening of influenza A. A TG was used to separate the signal in the first-order spectral images of the substrate; the system provided an excellent enhancement of the signal-to-noise ratio and high selectivity, and thus was further developed for multiplex analysis and single nucleotide polymorphism detection for other viruses.

3.3. Actual TSPR image acquisition (far-field effect, large area, long working distance)

A camera with a liquid crystal tunable filter was used in a TSPR setup as the detection system. Fig. 12(A) shows a typical setup used to acquire TSPR images (Lertvachirapaiboon et al., 2017a, 2017b). TSPR images of silver-coated grating substrates were recorded by this detection system at incident angles of the excitation light of 30–45°

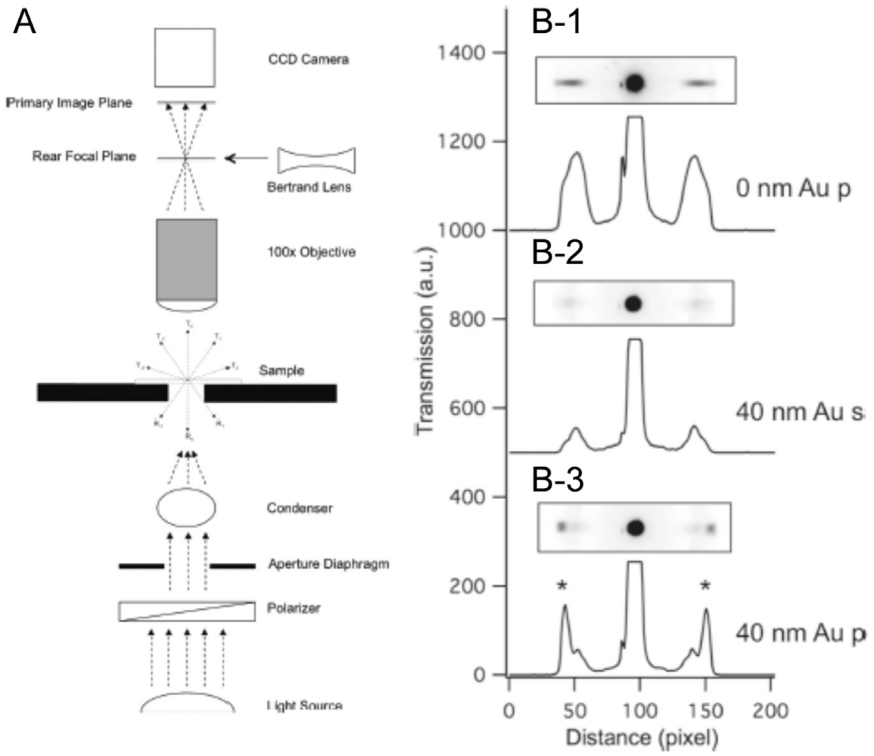

Fig. 10. (A) Schematic diagram of the optical configuration used for acquiring TSPR images at a normal angle. The optical configuration was used to measure TSPR signals through a gold-coated grating associated with direct and diffracted light (reflected and transmitted orders) using an optical microscope. (B) Transmitted intensity profiles for the gold-coated grating substrate: (B-1) uncoated grating observed under p-polarized light and gold-coated grating substrate (40-nm-thick gold layer) observed under (B-2) p- and (B-3) s-polarized light. The insets of the images in (B) show the corresponding optical diffraction images (inverted contrast) (Yeh et al., 2011).

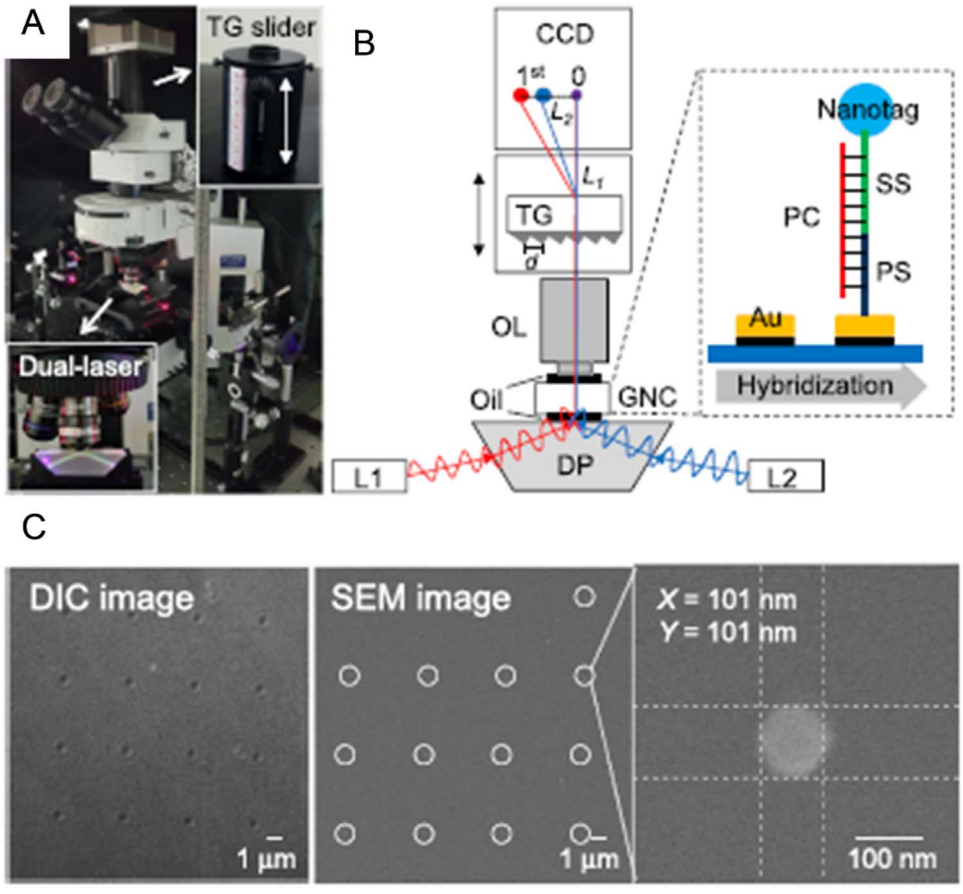

Fig. 11. (A) Physical layout and (B) schematic diagram of the SD-TIRS detection system containing the TG imaging system. (C) DIC and SEM images of a 4-by-4 array of gold nanopads with a pitch of 5 μm and a diameter of 100 nm fabricated using an electron beam lithography technique (Lee et al., 2017).

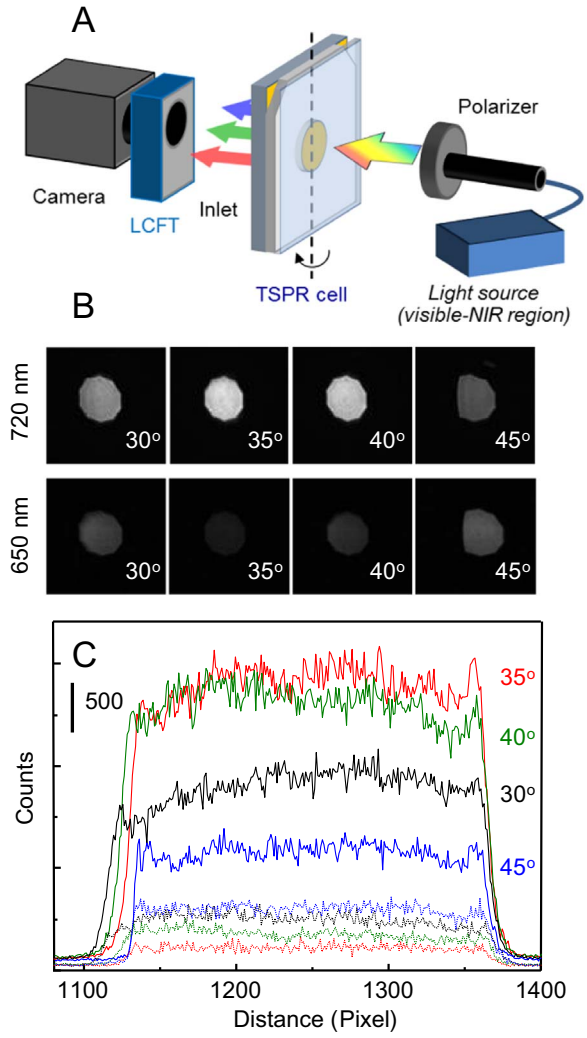

Fig. 12. (A) Schematic diagram of the experimental setup used for TSPR image acquisitions. (B) TSPR images and (C) TSPR intensities (*i.e.*, photon counts) at excitation wavelengths of 720 nm (with TSPR, solid line) and 650 nm (without TSPR, dashed line). The TSPR signals were measured at incident angles of the excitation light of 30–45°.

at a wavelength of 720 nm (*i.e.*, with TSPR); furthermore, the exposure time of the camera was fixed to 0.25 s. The results were subsequently compared with ones obtained at 650 nm (*i.e.*, without TSPR); the images of the two are shown side-by-side in Fig. 12(B). As can be seen in this figure, at an incident angle of 35°, the TSPR intensity at 720 nm was 10 times as large as the transmission intensity at 650 nm. As shown in the experimental setup in Fig. 12(A), this technique does not need to use high resolution imaging technologies. With respect to the TSPR phenomenon, the far-field signals were observed by the camera under specific wavelength, polarization, and angle of incidence conditions. This technique provides several practical advantages over other TSPR imaging techniques, because high-magnification optical microscopes are not needed for the monitoring of the light scattered by metal nanomaterials under dark-field and ATR conditions.

4. Enhanced TSPR signals using plasmonic nanostructures

Localized surface plasmon resonance (LSPR) from plasmonic structures has been used to facilitate and further excite the electric field at the surfaces of metal gratings in order to enhance the signal from such TSPR substrates (Jiang et al., 2007; Mock et al., 2008; Lertvachirapaiboon et al., 2013, 2014, 2017a, 2017b). The finite-difference time-domain (FDTD) method was used to simulate the electric field of a gold grating and of gold grating structures with gold nanoparticles (AuNPs) in order to monitor the enhancement of the TSPR signals. Fig. 13 shows the electric field of a typical water/rectangle gold grating model (gold layer thickness of 50 nm) with and without rectangular gold islands. In this study, the electric field was calculated under p-polarized light at a wavelength of 740 nm and at an incident angle of 35° in water. The gold islands were assumed to have nanostructures that were 10 nm wide and 5 nm high (Fig. 13(C)) and 100 nm wide and 10 nm high (Fig. 13(D)). These structures were similar to the dispersed AuNPs or aggregated AuNPs on gold grating films used in another study (Lertvachirapaiboon et al., 2013). This study utilized Palik parameters for the dielectric constant of gold (Palik (1985) Handbook of Optical Constants of Solid]. In Fig. 13(B), a strongly enhanced electric field can be observed on the gold surface exposed to water, which indicates the excitation of the surface plasmons. It should be noted that light was transferred through the continuous gold grating thin film; this can be seen in the near-field on the gold surface immediately adjacent to the polycarbonate. The electric field intensity was found to increase further when the gold islands existed on the gold grating, as shown in Fig. 13(C) and (D). The electric field enhancement observed from the gold grating structure with the gold islands was believed to be due to the interaction between propagating surface plasmons from the gold grating and the LSPR phenomenon from the gold islands (AuNPs). These results indicate that an enhancement in the near-field surface plasmon excitation can be obtained when a nanostructured surface is fabricated on a gold grating thin film, which thus enhances the TSPR signal.

An experimental study was also conducted into TSPR signals enhanced by LSPR, which investigated the effect that metal nanoparticles had on the gold-coated grating substrate; this was done *via* the growth of the metal nanoparticles on the gold grating surface. Furthermore, this work studied the distance-dependent LSPR effect on TSPR by controlling the distance between the metal nanoparticles and the surface of a gold grating (Lertvachirapaiboon et al., 2013, 2014). In order to grow the metal nanoparticles on the gold surface, AuNPs were directly grown on the gold surface, because we aimed to avoid any effects from the stabilizer used during AuNPs synthesis. A technique utilizing alcohol reduction was used to slowly grow AuNPs in order to produce a uniform coverage of AuNPs. In order to verify the presence of AuNPs on the gold surface, ultraviolet–visible light spectroscopy was used to monitor the characteristic LSPR peak of the LSPR spectrum at ~525 nm together with atomic force microscopy, which was used to measure changes in the average surface roughness (R_a) of the gold surface. The strong electric field on the surface of the gold-coated grating substrate containing AuNPs was verified by a layer-by-layer (LbL) technique that was used to deposit the polymer film. The TSPR intensity of this substrate increased significantly during LbL deposition until 6 bilayers of the LbL film (~12 nm) were deposited; with subsequent layers, only a slight increase in the TSPR intensity was observed (see Fig. 14(A)). With LSPR utilizing AuNPs, the propagation of the electric field into a dielectric layer was facilitated and its propagation distance increased. Furthermore, the extraordinary of the depth of the electric field appeared to be in agreement with the average size of the AuNPs (~9.7 nm). FDTD simulation results (Fig. 13) corroborated the experimental results, in that they showed that a stronger and larger electric field was obtained from the gold-coated grating substrate with AuNPs. In order to gain further insight into the LSPR phenomenon on TSPR, the distance between the metal nanoparticles and the gold grating surface was studied. The distance between these materials was controlled by LbL ultra-thin films of poly(diallydimethylammonium chloride)/poly(sodium 4-styrenesulfonate) and poly(allylamine hydrochloride)/poly(sodium 4-styrenesulfonate) (PAH/PSS). The coupling surface plasmon excitation between silver nanoparticles (AgNPs) and a gold grating substrate was showed strongest at a distance of 15–20 nm. As the PAH polymer was protonated/deprotonated, the PAH/PSS LbL film swelled/shrank

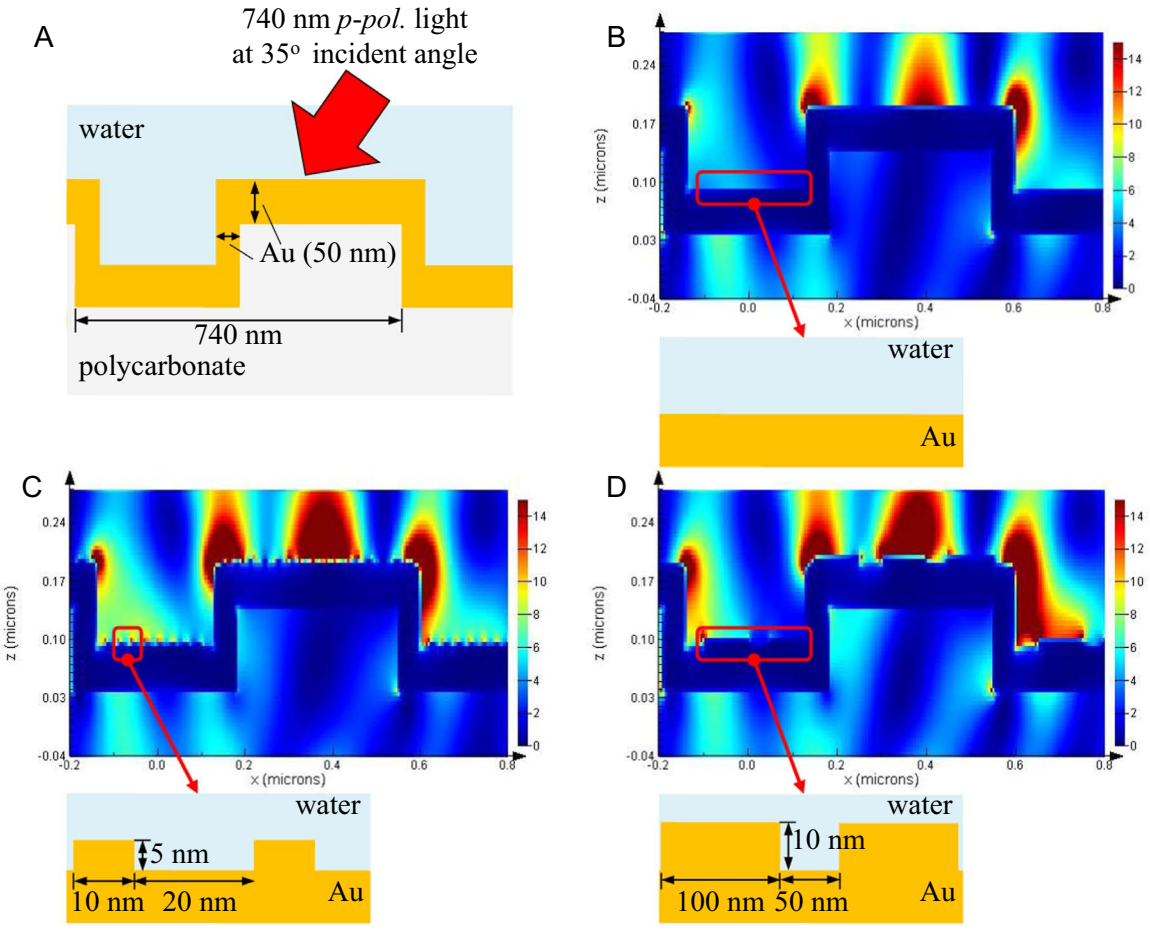

Fig. 13. (A) Schematic diagram of a gold grating film with a 50-nm-think gold-coated polycarbonate grating structure (grating pitch is 740 nm). (B) Electric field of the gold grating film, (C) gold grating film with small AuNPs, and (D) gold grating film with large AuNPs. The incident angle of the p-polarized light was 35°, and it impinged on the gold grating film in an aqueous environment. The color bar indicates the intensity of the electric field.

depending on the environmental pH. This technique was able to monitor the distance-dependent LSPR effect on the TSPR in real-time. The pH-switching behavior was investigated by alternately injecting pH 2 and 12 solutions into a TSPR cell. Under alkaline condition, PAH layers deprotonated, and the electrostatic interactions between the PAH layers and the AgNPs weakened in these conditions. The shrinkage of the intermediate layer induced a decrease in the TSPR intensity and a blue shift in the TSPR spectrum, because far-field transmission surface plasmons became scattering photons on the substrate surface. Under acidic conditions, however, the PAH layers became protonated, and an increase in the charge density was observed by the swelling of the polyelectrolyte layers; this resulted in an increase in the TSPR intensity. The corresponding results from (1) controlling the spacing thickness by changing the number of bilayers and (2) changing the spacing thickness *in situ* by adjusting the environmental pH are shown in Fig. 14. The changes in both the TSPR intensity and the wavelength of the TSPR peak are shown as a function of the number of bilayers (*i.e.*, the thickness of the spacer layer), and the transmission intensity under p-polarization during pH adjustment are shown in Fig. 14(B) and (C), respectively.

A TSPR imaging technique was used to investigate the effect of LSPR on TSPR. After silver nanoprisms (AgNPrs) were deposited on a functionalized silver-coated grating substrate, a decrease in the TSPR intensity could be observed (darker TSPR image, middle image in Fig. 13) from 2471.8 (black line in Fig. 15) to 1079.2 counts (red line in Fig. 15). In order to confirm that the change in the TSPR intensity was due to the effect of LSPR on the AgNPrs, 100 μM H_2O_2 was injected into the Teflon cell for 10 min. H_2O_2 is a powerful oxidizer, and it allowed for the AgNPrs to be oxidatively disintegrated by H_2O_2 into silver ions (Wongravee et al., 2013; Parnklang et al., 2013; Nitinaivinij et al., 2014; Lertvachirapaiboon et al., 2017a, 2017b). The brighter TSPR image in Fig. 13 (*i.e.*, the right-hand side image) and the increase in the TSPR signal (*i.e.*, the blue line in Fig. 13) indicated that the AgNPrs had been disintegrated due to the silver grating, with the AgNPrs being immersed in H_2O_2. These results also confirmed that the shift in the TSPR peak was caused by functionalized AgNPrs. A decrease of the TSPR intensity and a darker TSPR image at 720 nm were observed, because the TSPR excitation was shifted to a high wavelength after the AgNPrs were deposited before being shifted back after the dissolution of AgNPrs *via* H_2O_2 (Lertvachirapaiboon et al., 2017a, 2017b).

Other interesting techniques, such as long-range SPR and anti-reflection-coated grating substrates have been used to facilitate plasmon resonance and further increase the TSPR signal (Wang et al., 2013; Sharma et al., 2016; Shinbo et al., 2016). Long-range TSPR (LR-TSPR) has been observed on gold nanohole arrays (Sharma et al., 2016). The TSPR signals of the nanohole arrays were fine-tuned using a thermoresponsive hydrogel of cross-linked poly(N-isopropylacrylamide). The swelling/shrinking of the polymer network can be controlled by small temperature changes around the lower critical temperature of the hydrogel. When the gel collapsed, only conventional SPR signals could be observed at the individual interfaces, with no TSPR being observed. When the hydrogel was swollen, however, the TSPR was found to originate from long-range and short-range SPR. In a study on grating-coupling TSPR, TSPR based on the LR-SPR phenomenon was investigated. In order to demonstrate LR-TSPR on

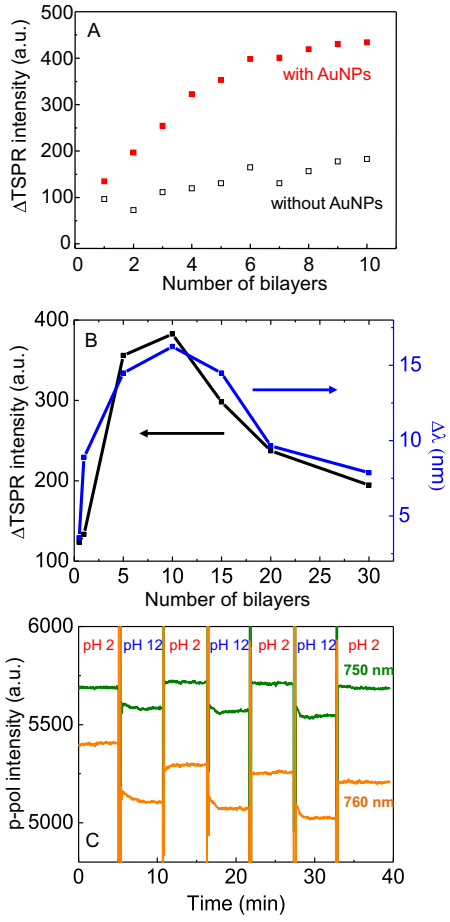

Fig. 14. (A) TSPR intensity during polymer film deposition on gold-coated grating substrates with (red filled squares) and without AuNPs (black open squares). (B) TSPR responses plotted as a function of the number of bilayer spacers. The distances between the metal nanoparticles and the metal grating surfaces were controlled by the protonation/deprotonation of the PAH polymer. (C) Kinetic curve of the gold-coated grating functionalized with $(PAH/PSS)_{10\ bilayers}$ + AgNPs when the pH inside the TSPR cells was switched from pH 2 to pH 12 for 3 cycles. The change in the TSPR intensity during the pH switching shows the effect of the distance between the metal nanoparticles and the metal grating surface. (For interpretation of the references to color in this figure legend, the reader is referred to the web version of this article.)

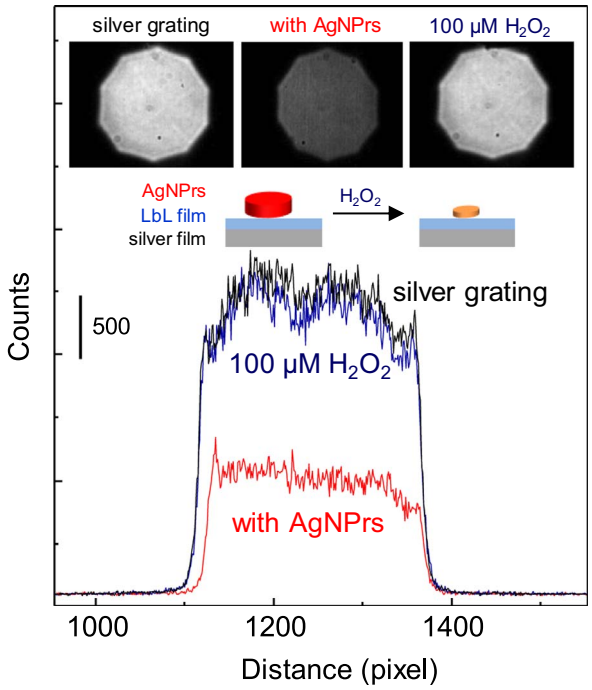

Fig. 15. TSPR images of a silver-coated grating substrate (left-hand side image), a silver-coated grating substrate with AgNPrs (middle image), and a silver-coated grating substrate with AgNPrs that had been soaked in 100 μM H_2O_2 for 10 min (right-hand side). The corresponding TSPR signals. All the TSPR images were recorded at an incident angle of 35° and at a wavelength of 720 nm in an aqueous environment.

a grating structure, a 500-nm-thick grating structure consisting of CYTOP was created by imprinting before coating the structure with a 30-nm-thick silver layer and a 5-nm-thick gold film (Shinbo et al., 2016). The TSPR spectrum of this substrate provided very strong optical transmission between wavelengths of 550–850 nm (this varied depending on the incident angle of the excitation light). The TSPR peak shift corresponded to the diffraction mode of $m = -1$. This substrate was also found to be very sensitive to changes in the thickness of the dielectric layer deposited on top of the metal layer.

5. TSPR technique for biosensor applications

TSPR techniques based on nanohole arrays have several advantages over conventional SPR techniques, such as having simple and flexible optical configurations, providing strong spectroscopic signals, and allowing for real-time signal monitoring (Liu et al., 2004; Brolo et al., 2004a, 2004b; Brolo et al., 2005; Leebeeck et al., 2007; Gordon et al., 2008; Sharpe et al., 2008; Escobedo et al., 2013; Wang et al., 2013; Song et al., 2015; Monteiro et al., 2016; Lee et al., 2016). TSPR techniques have therefore already been employed in several applications, in particular for biosensors. For example, a microfluidic chip-based gold nanohole array was used to monitor the biochemical affinity of a biotin–streptavidin system in real time (Leebeeck et al., 2007). The sensitive surface of the gold nanohole arrays was exploited to detect surface binding events during the assembly process of a cysteamine monolayer-biotin linker-streptavidin protein system. An average shift in the TSPR peak of up to 4 nm was observed. This result indicates that proteins adsorb onto the surfaces of gold nanohole arrays. Due to the high sensitivity of the peak shift during the adsorption process, this substrate could be used for a real-time monitoring in a biosensing system. Indeed, TSPR spectroscopy has been used to monitor the growth of bacteria as an antibiotic susceptibility test (Kee et al., 2013); the plasmonic nanohole arrays were used to quantitatively monitor bacterial growth and to test the susceptibility of *E.* coli to antibiotics. The sensor chip demonstrated that it was suitable for use for testing the susceptibility of *E.* coli to Ampicillin and Tetracycline at low bacterial quantities (< 100 cells) and showed significant results within a few hours. Fig. 16 shows the working principle for bacterial growth monitoring using the TSPR phenomenon with gold nanohole arrays and shows the significant shift of the TSPR peak when bacterial growth occurs.

Recently, nanohole array substrates have been employed for the multiplexed detection of *Chlamydia trachomatis* (CT) and *Neisseria gonorrhoeae* (NG), which are the two most common bacterial infections in urine (Soler et al., 2017). For this, a plasmonic microarray composed of gold nanohole sensor arrays was integrated into a microfluidic system. The disease-specific antibodies were used on different sensor arrays to selectively detect and quantify the bacteria in real-time. The detection limit was found to be 300 colony-forming units (CFU)/mL for CT and 1500 CFU/mL for NG. The results of this research showed that outstanding detection sensitivities could be achieved when measuring bacterial activity directly in a urine sample without DNA extraction or post-amplification steps being required. A schematic overview of the biosensor setup is shown in Fig. 17(A). The standard calibration for CT and NG in urine and a standard buffer solution are shown in Fig. 17(E) and (F), respectively.

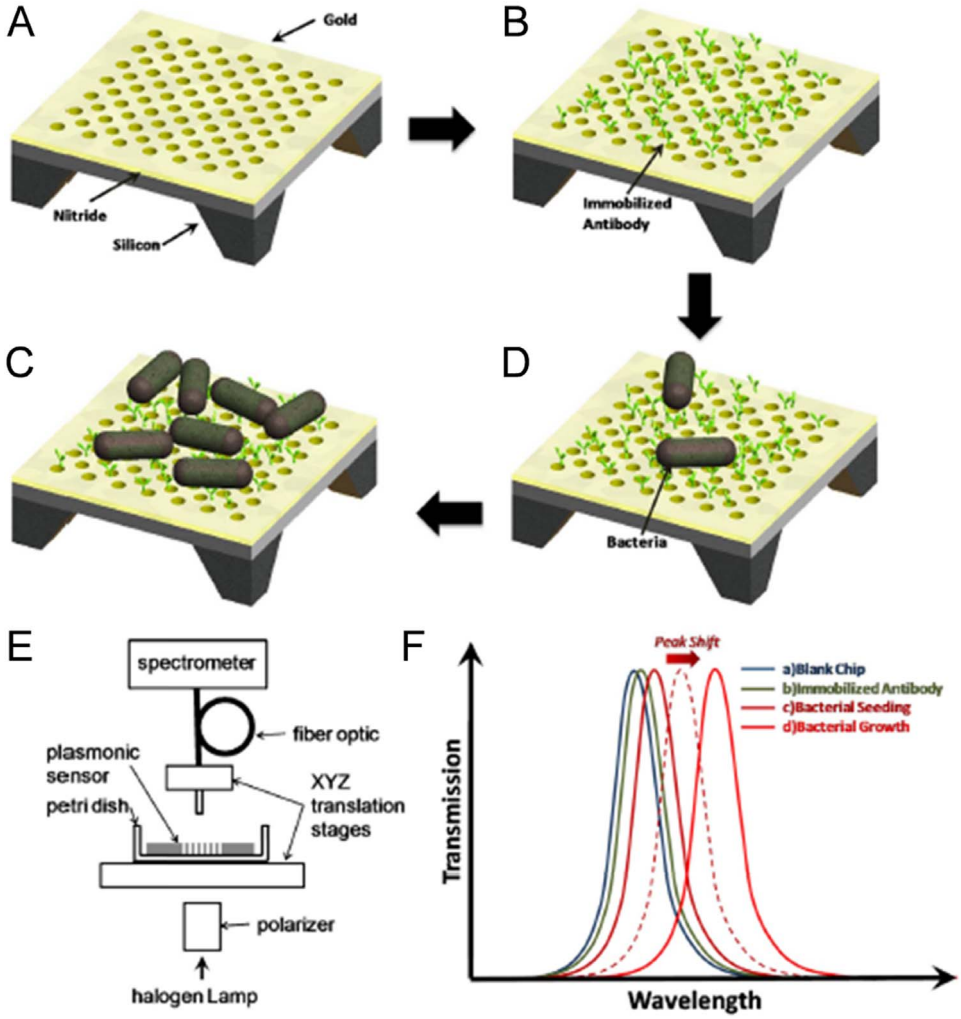

Fig. 16. Schematic illustration of a system for monitoring bacterial growth on gold nanohole arrays; (A) bare plasmonic nanohole sensor structure, (B) antibody immobilized on the sensor surface, (C) bacterial seeding on the substrate, and (D) monitoring of bacterial growth on the sensor chip. (E) Schematic of the experimental setup. (F) TSPR spectra of the gold nanohole arrays at various stages during the measurement (Kee et al., 2013).

To obtain a strong signal with high sensitivity that can be used for sensing, metal nanohole arrays were combined with plasmonic and fluorescent materials (Brolo et al., 2005; Sharpe et al., 2008; Escobedo et al., 2013; Wang et al., 2013; Song et al., 2015). For example, the plasmonic enhanced optical transmission of gold nanohole arrays has been used in biosensor applications; a small molecule of cortisol was detected using a cortisol-linker-thiol derivative. The combination of the plasmon effects of a gold nanohole array and AuNPs provided a three-fold increase in the TSPR peak shift over the use of a conventional substrate (Sharpe et al., 2008). A schematic diagram illustrating the binding steps for the detection of the cortisol-linker-thiol analyte is shown in Fig. 18(A) and the TSPR peak shifts for each step with and without primary antibodies being present is shown in Fig. 18(B).

Gold nanohole arrays have also been used to enhance fluorescence signals for biosensor applications. Several parameters have been investigated to maximize the fluorescence enhancement such as the distance between the fluorescent dyes and the metal surface overlap of the peak between the fluorophore and the plasmon excitation spectrum (Levene et al., 2003; Brolo et al., 2005; Brolo et al., 2006; Guo et al., 2010; Wu et al., 2011; Wang et al., 2013). Gold nanohole array substrates were used to enhance the fluorescence signal of oxazine 720, which is a fluorescent dye. The signal enhancement could be observed in the transmitted excitation spectra of gold nanohole arrays due to the surface plasmon excitation by the light source and a subsequent increase in the local electric field at the metal/dielectric interface. The enhancement factor for the fluorescence emission was found to be up to two orders of magnitude greater than the emission signal from a glass substrate (Brolo et al., 2005). Fig. 19 shows the integrated emission from the various arrays coated with a polyethylene film containing different concentrations of oxazine 720 for different laser excitation light sources. The results showed not only an enhancement of the total fluorescence emission, but also an improvement in the sensitivity. Aside from fluorescent dyes, quantum dots (QDs) have also been used to achieve fluorescence-enhanced TSPR (Brolo et al., 2006). The coupling of cadmium sulfide QDs to the TSPR of a metallic nanohole array showed an enhancement of the emission intensity by two orders of magnitude. The maximum of the enhancement was observed when the resonance from the nanohole array matched the photoluminescence peak of the QD. In 2011, the dependence of the enhanced fluorescence emission on the thickness of the fluorescent layer was investigated (Wu et al., 2011). The fluorescence emission intensity increased along with the thickness of the SiO_2 layer. When the thickness of the SiO_2 layer was increased by 1 nm, the metallic nanohole arrays, which had periodic structures based on periods of 550 and 500 nm, showed increases in their emission intensities of 1286 and 1125 units, respectively. The coupling of the excitation light to the SPR resulted in a strong electric field distribution near the fluorescent molecules; this could be more clearly observed when the thickness of the SiO_2 layer was increased. Another reason for the signal increase was due to a reduction in the fluorescence quenching; the fluorescence

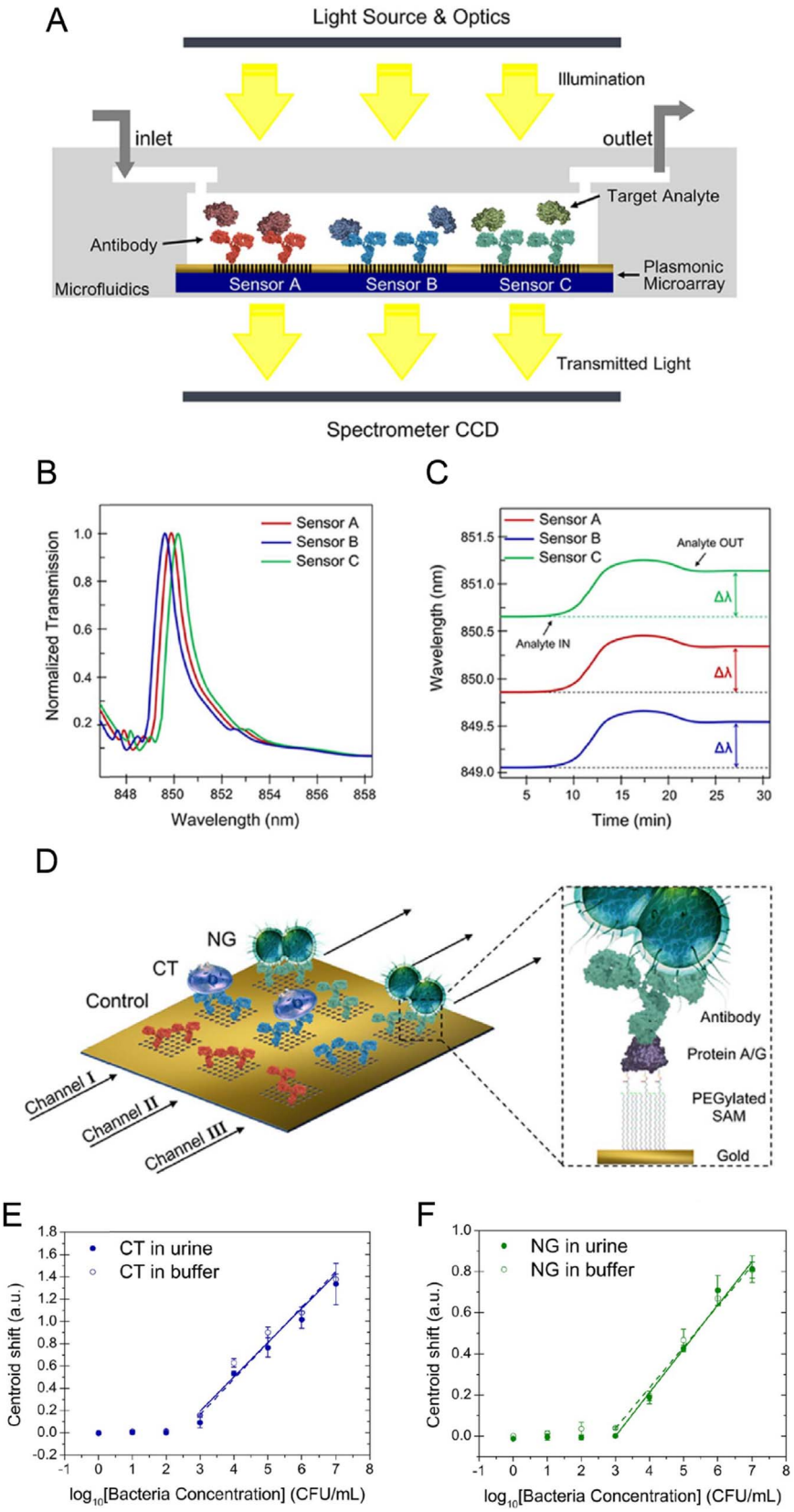

Fig. 17. (A) Schematic cross-sectional overview diagram of the biosensor structure. (B) Normalized TSPR spectrum acquired simultaneously from three different sensor arrays. (C) Real-time monitoring of the TSPR excitation wavelength shifts. (D) Schematic of the sensor surface biofunctionalization. The nanohole arrays were modified with different antibodies: anti-NG (green), anti-CT (blue), and a control antibody (red). The arrows indicate the liquid flow direction. The enlarged schematic diagram shown in panel (D) illustrates the surface chemistry strategy employed for the sensor functionalization. Standard calibrations for (E) CT and (F) NG in urine (solid line) and in a standard buffer solution (dashed line) are shown. Signals were obtained by flowing urine or buffer spiked with different concentrations of CT or NG over the antibody-functionalized sensor array (Soler et al., 2017). (For interpretation of the references to color in this figure legend, the reader is referred to the web version of this article.)

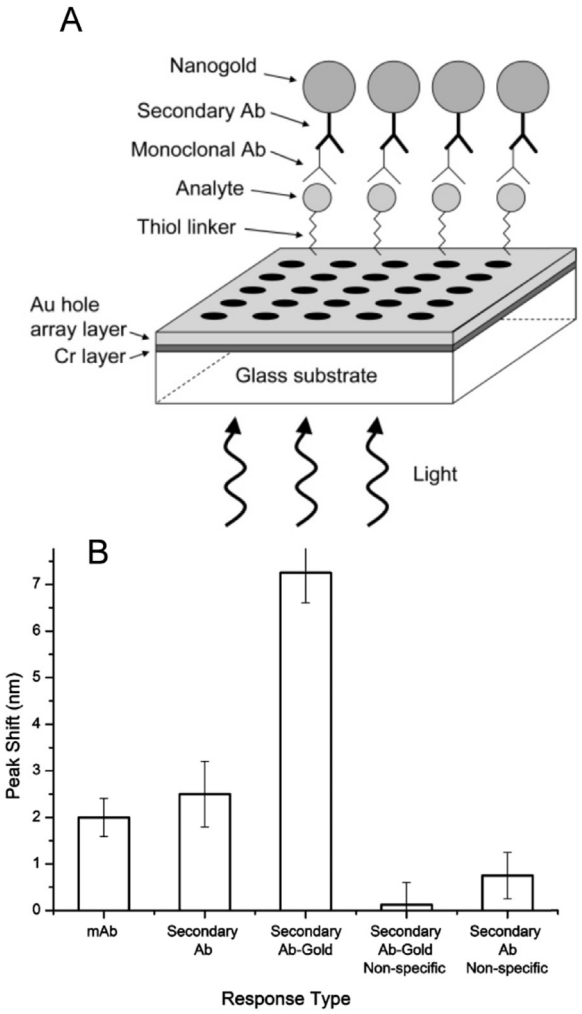

Fig. 18. (A) Schematic diagram of the binding steps for the detection of the cortisol-linker-thiol analyte, bound monoclonal antibody (mAb), and the secondary antibody-nanogold interaction. (B) TSPR peak shift for the primary antibody (mAb), the secondary antibody, and the secondary antibody-nanogold binding enhancement compared with the non-specific binding response for the secondary antibody and the secondary antibody-nanogold interaction in the absence of the primary mAb (Sharpe et al., 2008).

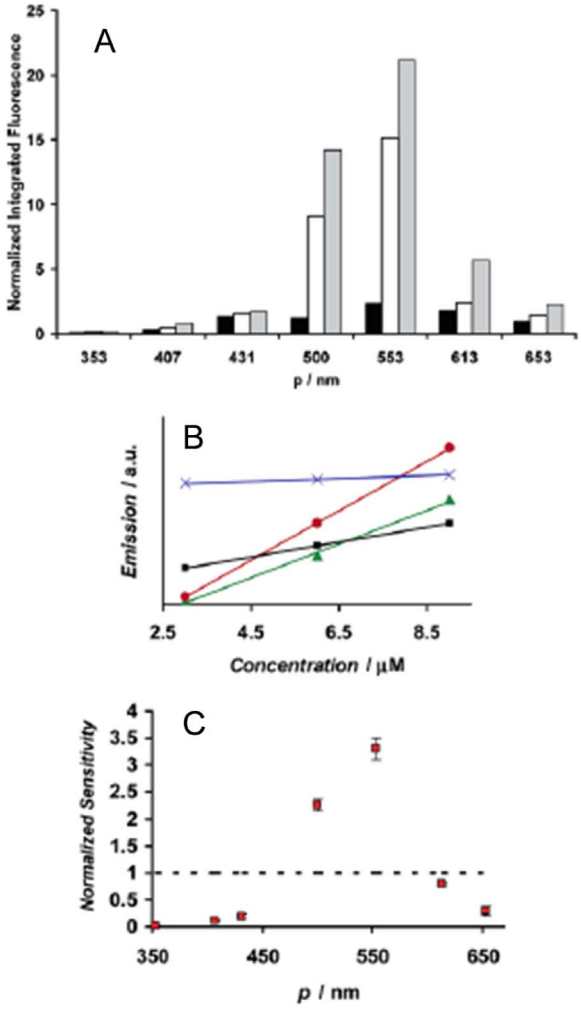

Fig. 19. Integrated fluorescence emission from arrays of nanoholes coated with polystyrene films doped with different concentrations of oxazine 720. The concentration of oxazine 720 is indicated by the black, white, and gray lines in panel (A); they were 3.2, 5.8, and 9.1 µM, respectively. (B) Integrated emission versus oxazine 720 concentration plots of polystyrene-doped films on glass slides (black, solid squares), polystyrene-doped films on an array of nanoholes with periodicity (p) of 431 (blue cross), 500 (green, solid triangle), and 553 nm (red, solid circle). (C) Sensitivity of the oxazine 720 films on the arrays with different periodicities normalized by the sensitivity obtained from the oxazine 720-coated glass slides. The dashed horizontal line at $S = 1$ corresponds to the sensitivity of the oxazine 720-coated glass slide (Brolo et al., 2005). (For interpretation of the references to color in this figure legend, the reader is referred to the web version of this article.)

quenching was found to decrease as the SiO_2 layer thickness increased. The enhancement of the fluorescent signal was further increased by the deposition of a photoresist layer on the gold-coated nanohole arrays; this increase was monitored as a function of the angle of incidence of the excitation light. These results showed that a fluorescence enhancement of up to 14 and 12 times could be achieved for the gold nanohole arrays at an incident angle of 70° and for the gold-coated photoresist nanohole arrays at an incident angle of 20°, respectively. The gold-coated photoresist nanohole arrays showed a three times higher sensitivity than when a substrate without a photoresist layer was used for the detection of a prostate-specific antigen immunoassay (Wang et al., 2013).

The enhancement of the fluorescence signal by plasmonic nanohole arrays for biosensor applications was explored for the detection of cancer markers (Escobedo et al., 2013). A TSPR-based nanohole array structure was used for the detection and subsequent quantification of an ovarian cancer marker; the monitoring system was based on an imaging technique. The detection limit and dynamic range for the TSPR nanohole array substrate used for the ovarian cancer marker were 5 nM and 0.25–9.0 µg/mL, respectively. Furthermore, a highly specific detection system consisting of a sandwiched bioassay was exploited for the detection of thrombin (Song et al., 2015). The sandwiched bioassay consisted of a primary aptamer/thrombin/secondary aptamer stack with QDs and was prepared on a gold nanohole array. Gold nanohole arrays with a pitch of 400 nm were fabricated *via* nanoimprinting using a nickel mold. The detection limit of this substrate for the detection of thrombin was 1 ng/mL, which is very close to that of single molecule detection. The ability of metallic nanohole arrays to enhance fluorescence signals is also employed in several techniques, such as for monitoring the thicknesses of ultra-thin films (Wu et al., 2011) and to enhance Raman spectroscopy signals (Brolo et al., 2004a, 2004b).

Grating-coupled TSPR techniques have also been developed for biosensor applications (Janmanee et al., 2012; Janmanee et al., 2013; Chuekachang et al., 2013a, 2013b; Chuekachang et al., 2013a, 2013b; Sriwichai et al., 2015). The carboxylic group of the conducting polymer poly(pyrrole-3-carboxylic acid) on a gold-coated grating substrate with gating acted as an active site for the functionalization of antibodies (Janmanee et al., 2012). In this study, immunoglobulin G (IgG) was detected, as shown in Fig. 20. Based on the swelling of the poly(pyrrole-3-carboxylic acid) (PP3C) film at different applied potentials, the

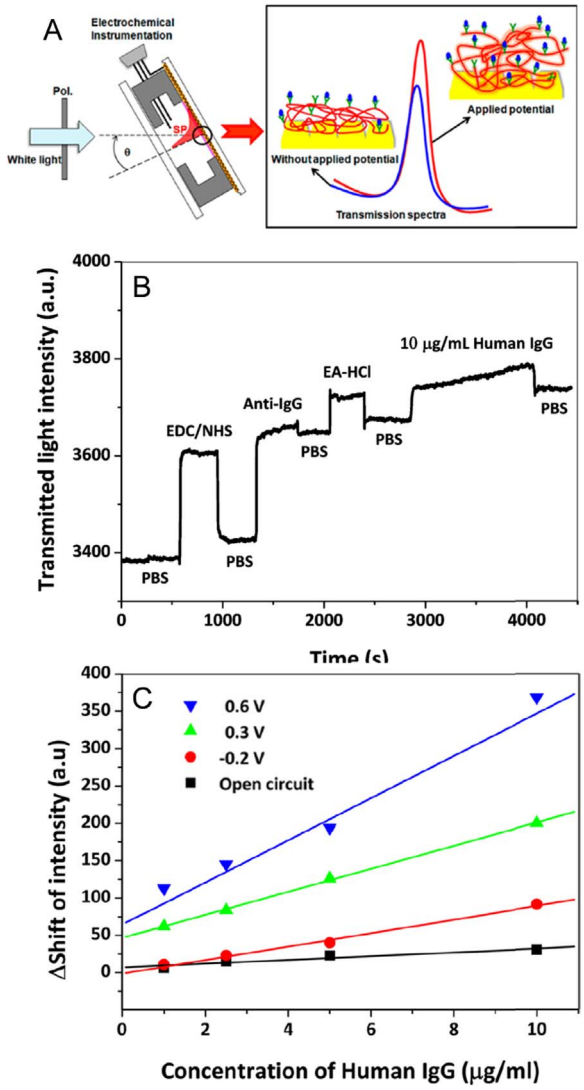

Fig. 20. (A) Schematic illustration of an EC-TSPR setup and typical TSPR intensity changes during detection. (B) TSPR binding curve during construction of a polymer PP3C film-based immunosensor for the detection of IgG (10 μg/mL). The experiment illustrated in panel (B) was conducted at an open circuit potential. (C) Plot of the shift in the transmission sensitivity during the binding process with IgG present at different applied constant potentials (Janmanee et al., 2012).

binding site was opened for the binding of anti-IgG and IgG, which increased the efficiency for this kind of immunosensor. An *in situ* study of electropolymerized poly(3-aminobenzoic acid) (PABA) on a gold-coated grating substrate for the label-free detection of IgG has also been investigated (Sriwichai et al., 2015). Electropolymerization was used to prepare a thin polymer film of PABA on a gold-coated grating substrate. The construction of the immunosensor when a constant potential was applied and at open circuit potential were investigated. After the applied potential had been maintained for a while, anti-IgG was injected into the TSPR cell and subsequently IgG was also injected. The preliminary results showed that the shift of the TSPR peak was sensitive to the injection of IgG. Recently, we reported on a TSPR measurement that could be used to detect glucose (Lertvachirapaiboon et al., 2017a, 2017b]; we developed a microfluidic TSPR sensor chip by assembling a gold-coated grating substrate with microchannels. The sensor chip displayed a strong TSPR signal between 650 and 800 nm. The maximum TSPR excitation was observed at an incident angle of 35°. The gold-coated grating substrate was functionalized with 3-mercapto-1-propanesulfonic acid, and subsequently a 5-bilayers of poly(allylamine hydrochloride)/poly(sodium 4-styrenesulfonate) was

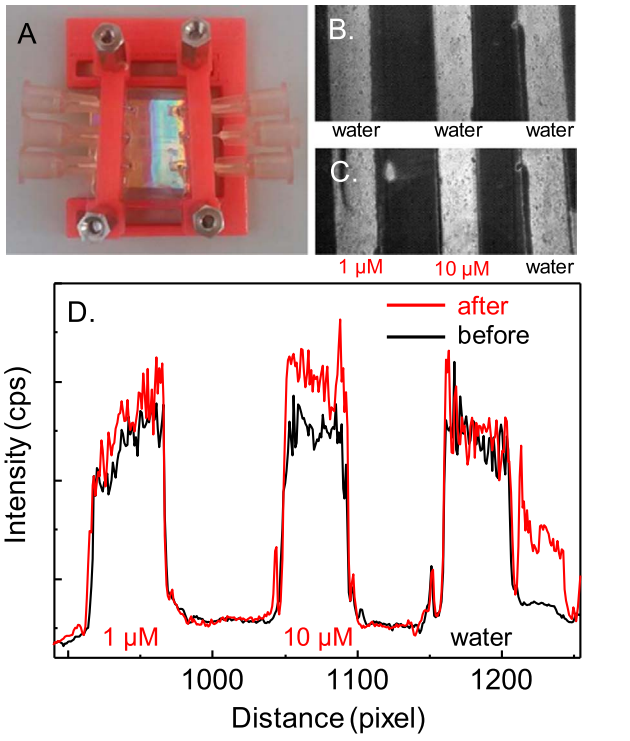

Fig. 21. (A) Photograph of a silver-coated three-channel microfluidic TSPR sensor chip; needles were inserted into the channel inlets. All of the parts were clamped down using a homemade clamp that was printed by a three-dimensional (3D) printer. TSPR images of the three-channel microfluidic cell (B) before and (C) after the injection of H_2O_2; panel (D) shows the corresponding TSPR intensities before (black line) and after (red line) the injection of H_2O_2. The TSPR signals were recorded as the water was injected at an incident angle of 35° and at an excitation wavelength of 720 nm in an aqueous environment. (For interpretation of the references to color in this figure legend, the reader is referred to the web version of this article.)

deposited on top to facilitate the coupling/decoupling of the surface plasmons and to prepare a uniform surface for sensing. The detection limit of the sensor chip was 2.31 mM for glucose. This technique has also been applied for other conducting polymers, such as poly(4-(3-pyrrole) butyric acid) (Janmanee et al., 2013), for similar antigen-antibody systems, and poly(2–aminobenzylamine) has been used for the detection of adrenaline and uric acid (Chuekachang et al., 2013a, 2013b; Chuekachang et al., 2013a, 2013b).

TSPR imaging can also be used for biosensor applications (Lertvachirapaiboon et al., 2017a, 2017b). Fig. 21 shows actual TSPR images and their corresponding TSPR intensities for the simultaneous detection of water and two different concentrations of H_2O_2. Water and aqueous solutions of H_2O_2 at concentrations of both 1 and 10 μM were simultaneously injected into microfluidic channels and left for 10 min; water was subsequently injected into all of the channels. A systematic decrease in the TSPR intensity was observed. A change in the TSPR intensity of the silver-coated grating substrate with AgNPrs from the detected channels with 1 and 10 μM H_2O_2 and water produced counts of 290.3, 653.6, and 27.1, respectively (the TSPR intensity from at least 30 pixels was averaged). These promising results strongly indicated that the TSPR imaging technique can be exploited in biosensor applications, particularly in combination with an oxidative enzyme system (*e.g.*, glucose oxidase, cholesterol oxidase, or reduced dihydro-nicotinamide adenine dinucleotide oxidase).

More recently, due to the high performances of smartphone cameras, they can be used to capture images as well as record VDO for further evaluation as part of a sensing protocol. Smartphones could therefore also be used in conjunction with TSPR techniques (Lee et al., 2016). A plasmonic grating sensor chip made from a cyclic olefin polymer was prepared *via* lithographic imprinting to detect pesticides.

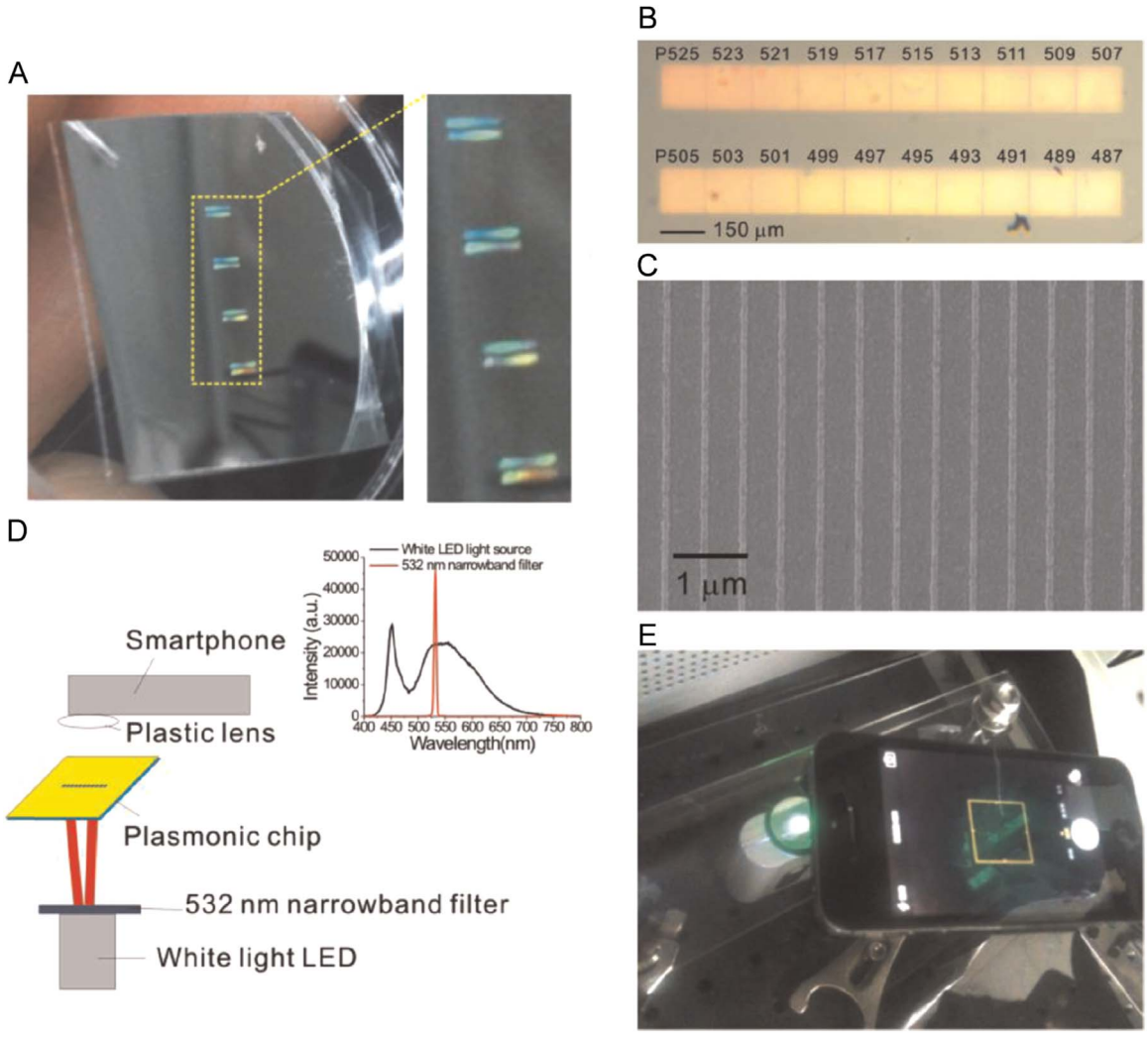

Fig. 22. (A) Photograph and enlarged image of the plasmonic biochips. (B) The transmitted light image of the biochips using white light as a light source. (C) SEM image of a nanoslit array with a period of 516 nm. (D) Schematic configuration of a portable optical system for image measurements; the system is composed of a smartphone, LED light source, and a narrowband filter. (E) Photograph of a detection system that uses a smartphone (Lee et al., 2016).

The sensitivity of the change in the optical signal was dependent on the concentration of the pesticide and could be recorded using a smartphone camera and subsequently estimated by eye. By recording the TSPR image and correctly evaluating the signals, this technique could be used to detect pesticides with a detection limit of 1 ppb. Fig. 22 shows the fabrication of plasmonic biochips and an optical setup in which a smartphone camera is used as a detector. This simple detection protocol is also low cost and label-free and does not require any expensive instruments; it therefore demonstrates that biosensing systems that monitor TSPR signals with a smartphone camera have the potential to emerge in the near future as a powerful detection technique.

6. Conclusions and outlooks

There are two main reasons as to why TSPR techniques have become useful for biosensor applications: firstly, the extraordinary transmission signals produced by TSPS substrates are strong and are highly sensitive to changes in local dielectric condition; secondly, the design of transmitting light setups are typically simple and flexible, which allows for them to be developed and modified further. The substrates themselves can be easily functionalized for specific analyzes. TSPR signals can be recorded by conventional spectrometers (at the range between ultraviolet and infrared light) and the detectors of camera. With a camera's detector, TSPR substrates are capable of carrying out multiplex detection of microfluidic channels. Nowadays, due to the high performance of the cameras in smartphones, the TSPR technique can be integrated into smartphones, which would allow for mobile devices to be developed that can carry out on-site detection, and point-of-care devices and household devices for practical biosensor applications can be developed. Because of the simple experimental setups and the strong signal-based SPR phenomenon of this technique, the technique can be coupled with imaging technologies. This technique also provides basic information with high resolution images, which can be further developed by mobile devices using smartphone cameras. The TSPR imaging technique is expected to become a powerful technique for biosensor applications that can combine imaging technologies with microfluidic technologies. Furthermore, due to 3D printing technology, prototypes of these devices can be produced in a laboratory. We intend to design and develop such devices; for example, the clamp used for the TSPR sensor chip in Fig. 21(A) was designed and printed by an in-house 3D printer they possess. 3D printing technology is expected to enable researchers to produce the parts needed to combine smartphones and sensor chips in the near future. Currently, several laboratories are not only able to detect target molecules, but also to develop devices that can have very high sensing performance levels; they can also develop prototypes. We believe that household biosensing devices will become a topic of particular interest

in the near future, and several powerful household biosensing devices with multiplex detection are expected to be developed that utilize smartphone applications for both signal evaluation and sample analysis.

Acknowledgments

This work was supported by JSPS KAKENHI Grant Number 16K13662, Japan (JSPS)-Thailand (NRCT) bilateral joint research program, and Niigata University U-go grant.

References

Baba, A., Matsuzawa, T., Sriwichai, S., Ohdaira, Y., Shinbo, K., Kato, K., Phanichphant, S., Kaneko, F., 2010. J. Phys. Chem. C 114, 14716–14721.
Baba, A., Aoki, N., Shinbo, K., Kato, K., Kaneko, F., 2011a. ACS Appl. Mater. Interfaces. 3, 2080–2084.
Baba, A., Wakatsuki, K., Shinbo, K., Kato, K., Kaneko, F., 2011b. J. Mater. Chem. 21, 16436–164441.
Baba, A., Tada, K., Janmanee, R., Sriwichai, S., Shinbo, K., Kato, K., Kaneko, F., Phanichphant, S., 2012. Adv. Funct. Mater. 22, 4383–4388.
Barnes, W.L., Murray, W.A., Dintinger, J., Devaux, E., 2004. Phys. Rev. Lett. 92, 107401.
Bian, T., Dong, B., Zhang, Y., 2012. Opt. Commun. 285, 1523–1527.
Bravo-Abad, J., García-Vidal, F.J., Martín-Moreno, L., 2004. Phys. Rev. Lett. 93, 227401.
Brolo, A.G., Gordon, R., Leathem, B., Kavanagh, K.L., 2004a. Langmuir 20, 4813–4815.
Brolo, A.G., Arctander, E., Gordon, R., Leathem, B., Kavanagh, K.L., 2004b. Nano Lett. 4, 2015–2018.
Brolo, A.G., Kwok, S.C., Moffitt, M.G., Gordon, R., Riordon, J., Kavanagh, K.L., 2005. J. Am. Chem. Soc. 127, 14936–14941.
Brolo, A.G., Kwok, S.C., Cooper, M.D., Moffitt, M.G., Wang, C.W., Gordon, R., Riordon, J., Kavanagh, K.L., 2006. J. Phys. Chem. B. 110, 8307–8313.
Chan, H.B., Marcet, Z., Carr, D., Bower, J.E., Cirelli, R., Ferry, E., Klemens, F.P., Miner, J.F., Pai, C.S., Taylor, J.A., 2005. Bell Labs Technical Journal 10, 143–150.
Chuekachang, S., Janmanee, R., Baba, A., Phanichphant, S., Sriwichai, S., Shinbo, K., Kato, K., Kaneko, F., Ushijima, H., 2013a. Mol. Cryst. Liq. Cryst. 580, 1–6.
Chuekachang, S., Janmanee, R., Baba, A., Phanichphant, S., Sriwichai, S., Shinbo, K., Kato, K., Kaneko, F., Ushijima, H., 2013b. Surf. Interface Anal. 45, 1661–1666.
Clark, A.W., Cooper, J.M., 2012. Angew. Chem. Int. Ed. 51, 3562–3566.
Crouse, D., Keshavareddy, P., 2007. Opt. Express 15, 1415–1427.
Degiron, A., Lezec, H.J., Yamamoto, N., Ebbesen, T.W., 2004. Opt. Commun. 239, 61–66.
Ebbesen, T.W., Lezec, H.J., Ghaemi, H.F., Thio, T., Wolff, P.A., 1998. Nature 391, 667–669.
Escobedo, C., Chou, Y.W., Rahman, M., Duan, X., Gordon, R., Sinton, D., Brolo, A.G., Ferreira, J., 2013. Analyst 138, 1450–1458.
Gao, H., Zheng, Z., Dong, A., Fan, Z., 2014. Optik 125, 6687–6690.
Guo, P.F., Wu, S., Ren, Q.J., Lu, J., Chen, Z., Xiao, S.J., Zhu, Y.Y., 2010. J. Phys. Chem. Lett. 1, 315–318.
Gordon, R., Sinton, D., Kavanagh, K.L., Brolo, A.G., 2008. Acc. Chem. Res. 41, 1049–1057.
Haftel, M.I., 2006. Appl. Phys. Lett. 88, 193104.
Hao, D., Takagi, M.O., Yamasaki, K., 2003. FEBS Lett. 536, 151–156.
Homola, J., Koudela, I., Yee, S.S., 1999. Sens. Actuators B 54, 16–24.
Janmanee, R., Baba, A., Phanichphant, S., Sriwichai, S., Shinbo, K., Kato, K., Kaneko, F., 2012. ACS Appl. Mater. Interfaces 4, 4270–4275.
Janmanee, R., Baba, A., Phanichphant, S., Sriwichai, S., Shinbo, K., Kato, K., Kaneko, F., 2013. Mol. Cryst. Liq. Cryst. 580, 29–34.
Jiang, G., Baba, A., Ikarashi, H., Xu, R., Locklin, J., Kashif, K.R., Shinbo, K., Kato, K., Kaneko, F., Advincula., R., 2007. J. Phys. Chem. C 111, 18687–18694.
Kang, X., Cheng, G., Dong, S., 2001. Electrochem. Commun. 3, 489–493.
Kee, J.S., Lim, S.Y., Perera, A.P., Zhang, Y., Park, M.K., 2013. Sens. Actuators B 182, 576–583.
Kim, M.W., Kim, T.T., Kim, J.E., Park, H.Y., 2009. Opt. Express 15, 12315–12322.
Knoll, W., 1998. Annu. Rev. Phys. Chem. 49, 569–638.
Koerkamp, K.J.K., Enoch, S., Segerink, F.B., Hulst, N.F., Kuipers, L., 2004. Phys. Rev. Lett. 92, 183901.
Krishnan, A., Thio, T., Kim, T.J., Lezec, H.J., Ebbesen, T.W., Wolff, P.A., Pendry, J., Martin-Moreno, L., Garcia-Vidal, F.J., 2001. Opt. Commun. 200, 1–7.
Lee, J.Y., Li, J., Yeung, E.S., 2007. Anal. Chem. 79, 8083–8089.
Lee, S., Park, G., Chakkarapani, S.K., Kang, S.H., 2015a. Biosens. Bioeletron. 63, 444–449.
Lee, S., Yu, H., Kang, S.H., 2015b. Chem. Comm. 51, 945–947.
Lee, K.L., Huang, J.B., Chang, J.W., Wu, S.H., Wei, P.K., 2015c. Sci. Rep. 5, 8547.
Lee, K.L., You, M.L., Tsai, C.H., Lin, E.H., Hsieh, S.Y., Ho, M.H., Hsu, J.C., Wei, P.K., 2016. Biosens. Bioelectron. 75, 88–95.
Lee, S., Chakkarapani, S.K., Yeung, E.S., Kang, S.H., 2017. Biosens. Bioelectron. 87, 842–849.
Leebeeck, A., Kumar, L.K.S., Lange, V., Sinton, D., Gordon, R., Brolo, A.G., 2007. Anal. Chem. 79, 4094–4100.
Lertvachirapaiboon, C., Supunyabut, C., Baba, A., Ekgasit, S., Thammacharoen, C., Shinbo, K., Kato, K., Kaneko, F., 2013. Plasmonics 8, 369–375.
Lertvachirapaiboon, C., Baba, A., Ekgasit, S., Thammacharoen, C., Shinbo, K., Kato, K., Kaneko, F., 2014. Plasmonics 9, 899–905.
Lertvachirapaiboon, C., Baba, A., Ekgasit, S., Shinbo, K., Kato, K., Kaneko, F., 2017a. Jpn. J. Appl. Phys. 56, 017002.
Lertvachirapaiboon, C., Baba, A., Ekgasit, S., Shinbo, K., Kato, K., Kaneko, F., 2017b. Sens. Actuators B 249, 39–43.
Levene, M.J., Korlach, J., Turner, S.W., Foquet, M., Craighead, H.G., Webb, W.W., 2003. Science 299, 682–686.
Lezec, H.J., Thio, T., 2004. Opt. Express 12, 3629–3651.
Li, Z., Clark, A.W., Cooper, J.M., 2016. ACS Nano 10, 492–498.
Liu, Y., Bishop, J., Williams, L., Blair, S., Herron, J., 2004. Nanotechnology 15, 1368–1374.
Lu, Y., Cho, M.H., Lee, Y., Rhee, J.Y., 2008. Appl. Phys. Lett. 93, 061102.
Luo, M., Liu, Q.H., Guo, J., 2010. J. Opt. Soc. Am. B 27, 560–566.
Mock, J.J., Hill, R.T., Degiron, A., Zauscher, S., Chilkoti, A., Smith, D.R., 2008. Nano Lett. 8, 2245–2252.
Monteiro, J.P., Oliveira, J.H., Radovanovic, E., Brolo, A.G., Girotto, E.M., 2016. Plasmonics 11, 45–51.
Nitinaivinij, K., Parnklang, T., Thammacharoen, C., Ekgasit, S., Wongravee, K., 2014. Anal. Methods 6, 9816–9824.
Palik, E.D., 1985. Handbook of Optical Constants of Solid. Academic, New York.
Parnklang, T., Lertvachirapaiboon, C., Pienpinijtham, P., Wongravee, K., Thammacharoen, C., Ekgasit, S., 2013. RSC Adv. 3, 12886–12894.
Petefish, J.W., Hillier, A.C., 2015. Anal. Chem. 87, 10862–10870.
Ren, X.F., Guo, G.P., Huang, Y.F., Wang, Z.W., Guo, G.C., 2007. Appl. Phys. Lett. 90, 161112.
Sharma, N., Keshmirit, H., Zhou, X., Wong, T.I., Petri, C., Liedberg, B., Dostalek, J., 2016. J. Phys. Chem. C 120, 561–568.
Sharpe, J.C., Mitchell, J.S., Lin, L., Sedoglavich, N., Blaikie, R.J., 2008. Anal. Chem. 80, 2244–2249.
Shinbo, K., Takizawa, K., Obata, N., Lertvachirapaiboon, C., Baba, A., Kato, Keizo, Kaneko, F., 2016. Polym. Bull. 73, 2539–2546.
Singh, B.K., Hillier, A.C., 2006a. Anal. Chem. 78, 2009–2018.
Singh, B.K., Hillier, A.C., 2006b. Anal. Chem. 78, 7335–7340.
Singh, B.K., Hillier, A.C., 2008. Anal. Chem. 80, 3803–3810.
Soler, M., Belushkin, A., Cavallini, A., Kebbi-Beghdadi, C., Greub, G., Altug, H., 2017. Biosens. Bioelectron. 94, 560–567.
Song, H.Y., Wong, T.I., Guo, S., Deng, J., Tan, C., Gorelik, S., Zhou, X., 2015. Sens. Actuators B 221, 207–216.
Sriwichai, S., Baba, A., Deng, S., Huang, C., Phanichphant, S., Advincula, R.C., 2008. Langmuir 24, 9017–9023.
Sriwichai, S., Baba, A., Phanichphant, S., Shinbo, K., Kato, K., Futao, K., 2015. Int. J. Polym. Sci. 2015, ID650516.
Sturman, B., Podivilov, E., Gorkunov, M., 2008. Phys. Rev. B 77, 075106.
Su, X., Zhang, J., 2004. Sens. Actuators B 100, 309–314.
Szabo, A., Stolz, L., Granzo, R., 1995. Curr. Opin. Struct. Biol. 5, 699–705.
Thio, T., Ghaemi, H.F., Lezec, H.J., Wolff, P.A., Ebbesen, T.W., 1999. J. Opt. Soc. Am. B 16, 1743–1748.
Wongravee, K., Parnklang, T., Pienpinijtham, P., Lertvachirapaiboon, C., Ozaki, Y., Thammacharoen, C., Ekgasit, S., 2013. Phys. Chem. Chem. Phys. 15, 4183–4189.
Wang, Y., Wu, L., Zhou, X., Wong, T.I., Zhang, J., Bai, P., Li, E.P., Liedberg, B., 2013. Sens. Actuators B 186, 205–211.
Wu, S., Guo, P., Huang, W., Xiao, S., Zhu, Y., 2011. J. Phys. Chem. C 115, 15205–15209.
Xie, S., Li, H., Fu, S., Xu, H., Zhou, X., Liu, Z., 2010. Opt. Commun. 283, 4017–4024.
Yeh, W.H., Kleingartner, J., Hillier, A.C., 2010. Anal. Chem. 82, 4988–4993.
Yeh, W.H., Petefish, J.W., Hillier, A.C., 2011. Anal. Chem. 83, 6047–6053.
Yeh, W.H., Hillier, A.C., 2013. Anal. Chem. 85, 4080–4086.
Zhang, W., Wnag, Y., Luo, L., Li, G., 2015. Plasmonics 10, 547–551.
Zhou, J., Guo, J., 2014. Sci. Rep. 4, 3614.